Characterization of Remote Sensing Albedo Over Sloped Surfaces Based on DART Simulations and In Situ Observations

Shengbiao Wu, Jianguang Wen, Dongqin You, Dalei Hao, Xingwen Lin, Qing Xiao, Qinhuo Liu, Jean-philippe Gastellu-Etchegorry

AGU100 ADVANCING EARTH AND SPACE SCIENCE

JGR

Journal of Geophysical Research: Atmospheres

RESEARCH ARTICLE
10.1029/2018JD028283

Key Points:
- Albedo measurements over sloped surfaces are significantly affected by the radiometer orientation
- Two commonly measured sloped surface albedos were characterized and analyzed using 3-D Discrete Anisotropic Radiative Transfer (DART) simulations and in situ observations over four typical slopes
- Both topographic parameters and atmospheric conditions affect the patterns of the horizontal and slope-parallel measured broadband albedos; using the DART simulations over different slopes, the absolute (relative) bias values between these two albedos can be up to 0.026 (61.8%), 0.134 (62.4%), and 0.114 (62.3%) in the visible (VIS), near-infrared (NIR), and shortwave (SW) bands, respectively

Supporting Information:
- Supporting Information S1

Correspondence to:
J. Wen,
wenjg@radi.ac.cn

Citation:
Wu, S., Wen, J., You, D., Hao, D., Lin, X., Xiao, Q., Liu, Q., & Gastellu-Etchegorry, J.-P. (2018). Characterization of remote sensing albedo over sloped surfaces based on DART simulations and in situ observations. *Journal of Geophysical Research: Atmospheres*, *123*, 8599–8622. https://doi.org/10.1029/2018JD028283

Received 4 JAN 2018
Accepted 2 JUL 2018
Accepted article online 12 JUL 2018
Published online 27 AUG 2018
Corrected 18 OCT 2018

This article was corrected on 18 OCT 2018. See the end of the full text for details.

Characterization of Remote Sensing Albedo Over Sloped Surfaces Based on DART Simulations and In Situ Observations

Shengbiao Wu[1,2], Jianguang Wen[1,2,3], Dongqin You[1,3], Dalei Hao[1,2], Xingwen Lin[1,2], Qing Xiao[1,3], Qinhuo Liu[1,2,3], and Jean-Philippe Gastellu-Etchegorry[4]

[1]State Key Laboratory of Remote Sensing Science, Institute of Remote Sensing and Digital Earth, Chinese Academy of Sciences, Beijing, China, [2]College of Resources and Environment, University of Chinese Academy of Sciences, Beijing, China, [3]Joint Center for Global Change Studies, Beijing, China, [4]Centre d'Etudes Spatiales de la BIOsphère-CNES, CNRS, IRD, Université de Toulouse, Toulouse, France

Abstract In situ albedo measurement over sloped surfaces is pivotal to a wide range of remote sensing applications, such as the estimation and evaluation of surface energy budget at regional and global scales. However, existing albedo measurements over rugged terrain are limited and controversial and remain a major challenge. In this paper, two commonly measured broadband albedos, which depend on incoming/outgoing geometric conditions, were characterized over sloped surfaces and illustrated. These albedos are the horizontal/horizontal sloped surface albedo (HHSA) and inclined/inclined sloped surface albedo (IISA). The 3-D Discrete Anisotropic Radiative Transfer (DART) model simulations over varying slopes were utilized to quantify differences in the albedos. In particular, the effects of the slope, aspect, the solar zenith angle, and the proportion of diffuse skylight were investigated. The results show that absolute (relative) biases between HHSA and IISA are significant, reaching up to 0.026 (61.8%), 0.134 (62.4%), and 0.114 (62.3%) in the visible, near-infrared, and shortwave broadbands, respectively. In addition, the diurnal cycle differences between HHSA and IISA were also compared using DART simulations and in situ observations over four typical slopes. Comparisons reveal that topographic parameters (e.g., slope and aspect) and atmospheric conditions (e.g., diffuse skylight and atmospheric visibility) are the primary factors, while the optical and structural parameters have a smaller effect.

1. Introduction

Surface albedo, defined as the ratio of radiation reflected from the target surface to the incident radiation on the surface (Liang et al., 1999), is well documented as one of the essential climate variables that control Earth's surface radiation and energy budget (Govaerts et al., 2008; Schaaf et al., 2009) and water and heat exchanges within the land surface-atmosphere system (Anderson et al., 2011; Liang et al., 2010; Mattar et al., 2014). Surface albedo is also a crucial indicator of regional and global climate change (Wang et al., 2007; Wang & Zeng, 2010), weather conditions (Boussetta et al., 2015; Stensrud, 2009), and agricultural production (Georgescu et al., 2011; Houspanossian et al., 2017).

Surface albedo is usually estimated from the integration of a surface reflectance anisotropy model characterized by the bidirectional reflectance distribution function (BRDF) (Schaepman-Strub et al., 2006) in hemispherical space (Lucht et al., 2000); Albedo is a function of surface optical and structural properties, terrain characteristics, wavelength, atmospheric conditions, and illumination geometry. Among these primary factors, the effect of heterogeneous topography creates great challenges, as the terrain impacts the surface albedo retrieved from airborne and satellite observations at both a fine spatial scale, such as a spatial resolution of tens of meters (Mayer et al., 2010; Painter et al., 2013; Schaaf et al., 1994; Wen et al., 2009), and a coarse spatial scale, such as kilometer-scale spatial resolution (Cherubini et al., 2017; Helbig & Löwe, 2012; Wen et al., 2014). Many studies have revealed that surface albedo is highly sensitive to terrain parameters (e.g., elevation, slope, aspect, and terrain shadow). For a snow-covered surface, as the elevation ranges from 3,200 to 4,200 m, surface albedo might increase from 0.27 to 0.67 due to the drop in the light-absorbing impurities (Painter et al., 2013). In a highly undulated terrain, surface albedo is dominated by subpixel topographies and shadows. For example, sloped surface with northern aspects have albedos that are smaller than those of southern slopes in winter and spring, as northern slopes are prone to be covered by shadows

(Cherubini et al., 2017). On the other hand, current routine satellite albedo retrieval algorithms always imply that Earth's surface is horizontally homogeneous (Schaaf et al., 2002; Diner et al., 2005; Qu et al., 2014). Some satellite sensors, such as the Multiangle Imaging SpectroRadiometer, directly exclude steep slopes greater than 20° using a topographic mask (Diner et al., 1999). Therefore, an accurate estimation of surface albedo over rugged terrain remains greatly challenging.

To evaluate the accuracy and uncertainty of airborne and satellite albedo products, the ground-based measurements are required as the direct or intermediate reference values (Román et al., 2010; Wu et al., 2017). As a physical parameter that is indirectly measured, surface albedo is usually approximated by the ratio of outgoing and incoming irradiances from the target surface using a radiometer with two back-to-back pyranometers (Wu et al., 2017). For a horizontally homogeneous surface, albedo is directly calculated as the ratio of two recorded irradiances. However, for a sloped surface, the incident and reflected irradiances are complex since these terms might be interpreted as horizontal or slope-parallel radiation depending on the radiometer orientation. Therefore, the measured surface albedo is greatly affected by sloped surfaces (Georg et al., 2016), which result in significant seasonal and diurnal surface radiative fluxes (Hoch & Whiteman, 2010; Serrano-Ortiz et al., 2016; Stiperski & Rotach, 2016; Weiser et al., 2016). Many studies reported that slope-parallel measured albedos provide consistent physical observations with respect to the surface energy budget (Georg et al., 2016; Hoch & Whiteman, 2010; Matzinger et al., 2003; Mayer et al., 2010; Weiser et al., 2016). However, almost all automatic weather stations and tower-based observations use horizontal radiometers to record long time series flux data sets (Mannstein, 1985), and most all albedo validation efforts focus on regions with horizontal surfaces (Román et al., 2010; Wang & Zeng, 2010; Wu et al., 2017). The differences in the interpretation of standard surface albedos result in great challenges for conducting albedo retrieval and validation, surface energy budget estimation, and climate model assessment over rugged mountainous areas (Van Angelen et al., 2012). Thus, it is necessary to investigate the albedo biases that arise from different interpretations of surface intrinsic reflectivity characterized by different radiometer orientations during the in situ measurements.

In this paper, we presented two common interpretations of measured albedos over sloped surfaces. These interpretations are named in terms of the orientation of the pyranometer that collects incident irradiance, followed by that of the pyranometer that observes reflected irradiance: horizontal/horizontal sloped surface albedo (HHSA) and inclined/inclined sloped surface albedo (IISA). The physical understandings and mathematical quantifications of measured albedos were provided. To illustrate and analyze topographic effects on surface albedos, 3-D Discrete Anisotropic Radiative Transfer (DART) simulations over varying slopes and in situ measurements over four typical slopes were used. Particularly, the diurnal cycle patterns of surface albedo associated with different slopes, aspects, structural parameters and atmospheric conditions were explored.

2. Albedo Mathematic Quantifications Over a Sloped Surface

2.1. Common Albedo Definitions Used by Remote Sensing Community

Surface albedo $a(\Omega_s, \lambda)$ is expressed as

$$a(\Omega_s, \lambda) = \frac{E_r(\Omega_s, \lambda)}{E_i(\Omega_s, \lambda)} \tag{1}$$

where subscripts i and r represent the incidence and reflection, respectively. Ω_s is the solar geometry defined by the solar zenith angle (SZA) θ_s and the solar azimuth angle φ_s. $E_i(\Omega_s, \lambda)$ and $E_r(\Omega_s, \lambda)$ are the incident and reflected irradiances (W/m^2) at wavelength λ, respectively.

As shown in Figure 1a, for a horizontal surface, the incident irradiance includes three parts: (1) the direct solar radiation E_s, which is determined by the latitude, the solar hour angle, the elevation, and the exact ground location relative to the Sun; (2) the diffuse skylight E_d, which is affected by the atmospheric clouds, the water vapor content, and the aerosol particles (Chen et al., 2006); and (3) the adjacency effect E_c that comes from adjacent objects. Consequently, surface albedo in equation (1) is quantified as

$$a(\Omega_s, \lambda) = \frac{E_{rs} + E_{rd} + E_{rc}}{E_s + E_d + E_c} \tag{2}$$

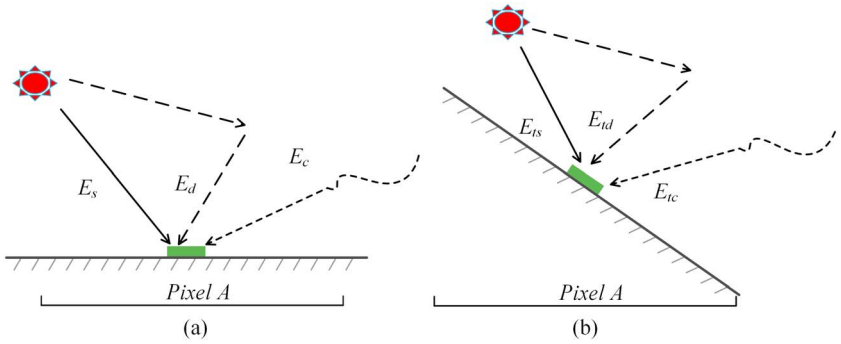

Figure 1. Schematic representation of radiative flux components over a (a) horizontal and (b) sloped surface.

When only direct solar radiation is involved, the calculated albedo is referred to as directional-hemispheric reflectance (also known as black-sky albedo; Schaepman-Strub et al., 2006). If only diffuse skylight is considered, the derived albedo is referred to as bihemispherical reflectance (also known as white-sky albedo; Schaepman-Strub et al., 2006). Under realistic conditions, if the direct solar radiation and diffuse skylight are both considered as downward radiation, the retrieved albedo is known as blue-sky albedo.

Similarly, the surface albedo of a sloped surface (Figure 1b) is modeled as

$$a(\Omega_s, \mathrm{DEM}, \lambda) = \frac{E_{trs} + E_{trd} + E_{trc}}{E_{ts} + E_{td} + E_{tc}} \tag{3}$$

where subscript t represents the local geometry over a sloped surface. DEM indicates the topographic parameters provided by digital elevation or terrain models. Compared with a horizontal surface, the direct solar

Table 1
Radiometer Orientations in Surface Albedo Measurements

	Flat surface	Sloped surface	
Topography type			
Incoming/Viewing	*Horizontal*	*Horizontal*	*Inclined*
Horizontal	*Horizontal-horizontal* CASE 1 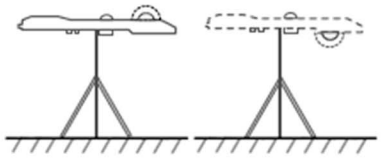	*Horizontal-horizontal* CASE 2 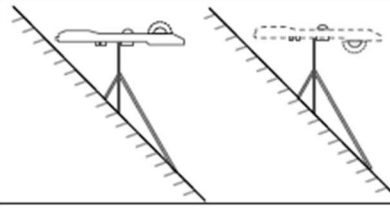	*Horizontal-inclined* CASE 3 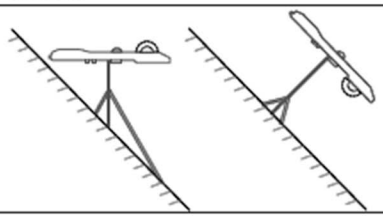
Inclined		*Inclined-horizontal* CASE 4 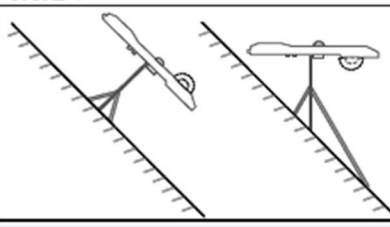	*Inclined-inclined* CASE 5 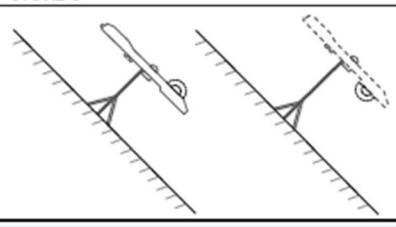

Note. First and second columns represent the incidence and reflection, respectively. Dashed radiometers in CASE 1, CASE 2, and CASE 5 indicate single-beam modes.

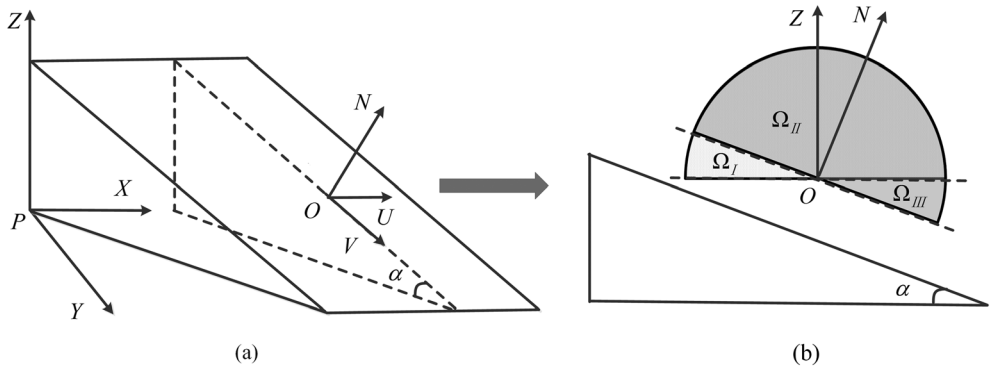

Figure 2. Spatial reference frames for albedo measurement over a sloped surface with (a) oblique and (b) side views. *O-UVN* and *P-XYZ* are the slope and horizontal coordinates, respectively.

radiation E_{ts} of a sloped surface is regulated by an altered local incident geometry, and topographic occlusions cause the diffuse skylight E_{td} to decrease and adjacent slope-reflected irradiance E_{tc} to increase. Thus, an accurate quantification of radiative components is a prerequisite for albedo characterization for sloped surfaces.

2.2. Radiative Flux Components Over a Sloped Surface

As shown in Figure 1b, E_{ts} over a sloped surface is modeled as the product of solar irradiance E_s and local SZA θ_{ts}.

$$E_{ts} = \Theta_s E_s \frac{\cos\theta_{ts}}{\cos\theta_s} \tag{4}$$

where Θ_s is a binary quantity that indicates whether the target slope is sunlit.

E_{td} over a sloped surface is modeled as

$$E_{td} = E_d V_d \tag{5}$$

where V_d is the sky-view factor, which is usually approximated as $\frac{1}{2}(1 + \cos\alpha)$ with isotropic diffuse skylight (Dozier & Frew, 1990), where α is slope.

Similarly, E_{tc} over a sloped surface is calculated as

$$E_{tc} = E_c V_c \tag{6}$$

where V_c is the terrain-view factor, which is complementary to the sky-view factor and estimated as $\frac{1}{2}(1 - \cos\alpha)$ (Dozier & Frew, 1990) with the isotropic irradiance reflected from adjacent slopes.

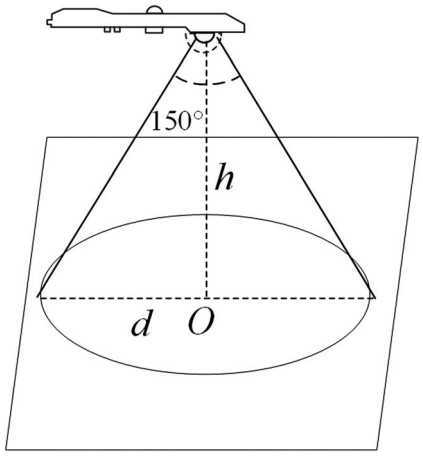

Figure 3. Schematic representation of a radiometer field of view. *h* is the pyranometer height, and *d* is the effective diameter. The $h \approx 8.7\,d$ to account for 95% of surface reflected irradiance (Sailor et al., 2006).

2.3. Surface Albedo Measurements Over a Sloped Surface

Table 1 lists five radiometer orientations that might occur in surface albedo measurements. For a horizontal surface (CASE 1), albedo is explicitly estimated by the ratio of downwelling and upwelling irradiances collected by a horizontal radiometer. This measured albedo is called the horizontal/horizontal flat surface albedo (HHFA). For a sloped surface, when the radiometer is horizontally positioned (CASE 2), the measured albedo is named the HHSA. When the radiometer is inclined to slope-parallel (CASE 5), the measured albedo is named the IISA. These albedos are usually measured during field observations by a single-beam mode (Milton et al., 2009) using a radiometer with two opposing pyranometers (e.g., CNR4 net radiometer, Kipp & Zonen, Netherlands),

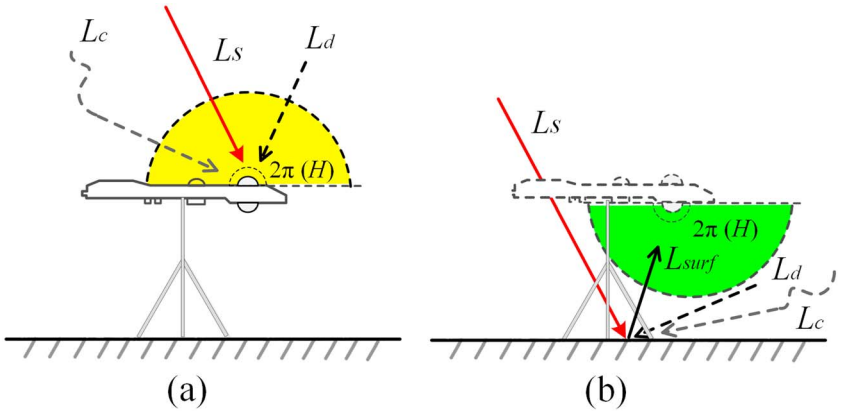

Figure 4. Radiative flux components of a horizontal radiometer over a horizontal surface in the (a) incidence and (b) reflection. L_s, L_d, L_c, and L_{surf} are the direct, sky, adjacent target-reflected, and target surface-reflected radiances, respectively.

such as the flux tower networks. According to the interpretations of in field observations incoming and outgoing irradiances, sloped surface albedo also may be measured by another two horizontal/inclined radiometers (CASE 3) or two inclined/horizontal instruments (CASE 4). Under this circumstance, a double-beam mode (Matzinger et al., 2003) with two separate pyranometers (e.g., CMP21, Kipp & Zonen, Netherlands) is required to simultaneously measure the downwelling and upwelling irradiances. In this study, we focus on HHSA and IISA, as they are directly linked with the current satellite products or the surface intrinsic reflection property.

One of the effects of radiometer orientation on surface irradiance is that it separates the whole sky (4π) into two parts, that is, upward and downward sloped hemispheres for a sloped surface and upward and downward horizontal hemispheres for a horizontal surface. These spatial separations are consistent with two space reference frames: slope coordinates *O-UVN* and horizontal coordinates *P-XYZ* (Figure 2a), which include three subdivisions, Ω_I, Ω_{II}, and Ω_{III} (Figure 2b). In particular, Ω_{II} is shared by *P-XYZ* and *O-UVN*. The upward sloped hemisphere $2\pi(S)$ includes Ω_{II} above the horizon and Ω_{III} under the horizon (i.e., $2\pi(S) = \Omega_{II} + \Omega_{III}$), and the upward horizontal hemisphere $2\pi(H)$ contains Ω_I and Ω_{II} (i.e., $2\pi(H) = \Omega_I + \Omega_{II}$).Similarly, the downward hemispheres have the same subdivisions. Thus, we treat them like we treat the upward hemispheres in the following sections.

The field of view (FOV) of a pyranometer (e.g., CASE 1 in Table 1) is required to be 180° to ensure that the radiation is collected from the whole hemisphere. However, owing to limitations in manufacturing, radiometers usually have downward pyrgeometers with much smaller FOVs (e.g., 150° in Figure 3), which collect approximately 95% of the surface reflected irradiance (Sailor et al., 2006). In this study, we still assume that radiometer FOV is 180° because surface reflected irradiance within the missing FOV has a small contribution (<5%) to the global radiation due to the cosine effect, and these underestimations are compensated in the calibration procedure.

2.3.1. Horizontal/Horizontal Flat Surface Albedo

The measured albedo in CASE 1 (Table 1) is consistent with current remote sensing albedo retrieval algorithms, which assume that the target surface is horizontally homogeneous and smooth. Considering that the adjacent effect (Figure 4) is relatively small, approximately 5% in the global incident irradiance (Ryu et al., 2018), this component is usually neglected. Thus, the downwelling radiance arriving at radiometer $L_i^{HHF}(\Omega_i)$ at solid angle Ω_i is expressed as

$$L_i^{HHF}(\Omega_i) = L_s\delta(\Omega_i - \Omega_s) + L_d(\Omega_i) \tag{7}$$

where L_s and $L_d(\Omega_i)$ are the direct solar radiance and the sky radiance, respectively. The term $\delta(\Omega_i - \Omega_s)$ in equation (7) is the Dirac delta function. It is a selector function for mathematical integral, which is 0 everywhere except at the solar direction $\Omega_s(\theta_s, \varphi_s)$ where it is infinite, to ensure a parallel beam of incident solar radiation.

$$\delta(\Omega_i-\Omega_s)=\begin{cases}\infty & \Omega_i=\Omega_s\\ 0 & \Omega_i\neq\Omega_s\end{cases}\quad\text{and}\int_{2\pi(H)}\delta(\Omega_i-\Omega_s)\mathrm{d}\Omega_i=1 \tag{8}$$

Thus, the hemispheric downwelling irradiance $E_i^{\mathrm{HHF}}(\Omega_s)$ and hemispheric upwelling irradiance $E_r^{\mathrm{HHF}}(\Omega_s)$ reaching the radiometer are calculated as

$$E_i^{\mathrm{HHF}}(\Omega_s)=\int_{2\pi(H)}L_i^{\mathrm{HHF}}(\Omega_i)\cos\theta_i\mathrm{d}\Omega_i=\int_{2\pi(H)}(L_s\delta(\Omega_i-\Omega_s)+L_d(\Omega_i))\cos\theta_i\mathrm{d}\Omega_i \tag{9}$$

$$\begin{aligned}E_r^{\mathrm{HHF}}(\Omega_s)&=\frac{1}{\pi}\int_{2\pi(H)}\rho(\Omega_i,\Omega_r)E_i^{\mathrm{HHF}}(\Omega_i)\cos\theta_r\mathrm{d}\Omega_r\\&=\frac{1}{\pi}\int_{2\pi(H)}\int_{2\pi(H)}\rho(\Omega_i,\Omega_r)(L_s\delta(\Omega_i-\Omega_s)+L_d(\Omega_i))\cos\theta_i\cos\theta_r\mathrm{d}\Omega_i\mathrm{d}\Omega_r\end{aligned} \tag{10}$$

where $\rho(\Omega_i,\Omega_r)$ is the bidirectional reflectance factor (BRF), which is equal to πBRDF.

HHFA, defined as the ratio of the radiative flux reflected by a horizontal surface to incident radiative flux, is modeled as

$$\begin{aligned}\mathrm{HHFA}=\alpha^{\mathrm{HHF}}(\Omega_s)&=\frac{E_r^{\mathrm{HHF}}(\Omega_s)}{E_i^{\mathrm{HHF}}(\Omega_s)}=\frac{\frac{1}{\pi}\int_{2\pi(H)}\int_{2\pi(H)}\rho(\Omega_i,\Omega_r)(L_s\delta(\Omega_i-\Omega_s)+L_d(\Omega_i))\cos\theta_i\cos\theta_r\mathrm{d}\Omega_i\mathrm{d}\Omega_r}{\int_{2\pi(H)}(L_s\delta(\Omega_i-\Omega_s)+L_d(\Omega_i))\cos\theta_i\mathrm{d}\Omega_i}\\&=\frac{\frac{1}{\pi}\int_{2\pi(H)}\int_{2\pi(H)}\rho(\Omega_i,\Omega_r)L_s\delta(\Omega_i-\Omega_s)\cos\theta_i\cos\theta_r\mathrm{d}\Omega_i\mathrm{d}\Omega_r}{\int_{2\pi(H)}L_s\delta(\Omega_i-\Omega_s)\cos\theta_i\mathrm{d}\Omega_i+\int_{2\pi(H)}L_d(\Omega_i)\cos\theta_i\mathrm{d}\Omega_i}\\&\quad+\frac{\frac{1}{\pi}\int_{2\pi(H)}\int_{2\pi(H)}\rho(\Omega_i,\Omega_r)L_d(\Omega_i)\cos\theta_i\cos\theta_r d\Omega_i d\Omega_r}{\int_{2\pi(H)}L_s\delta(\Omega_i-\Omega_s)\cos\theta_i\mathrm{d}\Omega_i+\int_{2\pi(H)}L_d(\Omega_i)\cos\theta_i\mathrm{d}\Omega_i}\end{aligned} \tag{11}$$

Compared with the isotropic diffuse skylight, a slight improvement will occur (e.g., 0.1–2.0% relative error for the Moderate Resolution Imaging Spectroradiometer product; Román et al., 2010) when anisotropic diffuse illumination is adopted, except under high SZAs or extremely turbid atmospheres (e.g., 10% relative bias, Román et al., 2010). Thus, it is reasonable to adopt isotropic sky radiance to simplify equation (11), where $E_d=\int_{2\pi(H)}L_d(\Omega_i)\cos\theta_i\mathrm{d}\Omega_i=\pi L_d$. Owing to the sampling property of the Dirac delta function, $E_s=\int_{2\pi(H)}L_s\delta(\Omega_i-\Omega_s)\cos\theta_i\mathrm{d}\Omega_i=L_s\cos\theta_s$. Consequently, HHFA is estimated as

$$\begin{aligned}\mathrm{HHFA}=\alpha^{\mathrm{HHF}}(\Omega_s)&=\frac{\frac{1}{\pi}E_s\int_{2\pi(H)}\rho(\Omega_s,\Omega_r)\cos\theta_r\mathrm{d}\Omega_r}{E_s+E_d}+\frac{\frac{1}{\pi^2}E_d\int_{2\pi(H)}\int_{2\pi(H)}\rho(\Omega_i,\Omega_r)\cos\theta_i\cos\theta_r\mathrm{d}\Omega_i\mathrm{d}\Omega_r}{E_s+E_d}\\&=(1-f)\frac{1}{\pi}\int_{\Omega_I+\Omega_{II}}\rho(\Omega_s,\Omega_r)\cos\theta_r\mathrm{d}\Omega_r+f\frac{1}{\pi^2}\int_{\Omega_I+\Omega_{II}}\int_{\Omega_I+\Omega_{II}}\rho(\Omega_i,\Omega_r)\cos\theta_i\cos\theta_r\mathrm{d}\Omega_i\mathrm{d}\Omega_r\\&=(1-f)\alpha_{\mathrm{bs}}^{\mathrm{HHF}}(\Omega_s)+f\alpha_{\mathrm{ws}}^{\mathrm{HHF}}\end{aligned} \tag{12}$$

where f represents the fraction of diffuse skylight. $\alpha_{\mathrm{bs}}^{\mathrm{HHF}}(\Omega_s)$ and $\alpha_{\mathrm{ws}}^{\mathrm{HHF}}$ are the black-sky and white-sky albedos, which adhere to the following equations:

$$\alpha_{\mathrm{bs}}^{\mathrm{HHF}}(\Omega_s)=\frac{1}{\pi}\int_{\Omega_I+\Omega_{II}}\rho(\Omega_s,\Omega_r)\cos\theta_r\mathrm{d}\Omega_r \tag{13}$$

$$\alpha_{\mathrm{ws}}^{\mathrm{HHF}}=\frac{1}{\pi^2}\int_{\Omega_I+\Omega_{II}}\int_{\Omega_I+\Omega_{II}}\rho(\Omega_i,\Omega_r)\cos\theta_i\cos\theta_r\mathrm{d}\Omega_i\mathrm{d}\Omega_r \tag{14}$$

2.3.2. Horizontal/Horizontal Sloped Surface Albedo

As shown in CASE 2 (Table 1), when the radiometer is positioned horizontally over a sloped surface, the incident irradiance includes three parts (Figure 5) similar to those in equation (7) but with topographic occlusion. Similarly, the downward radiance $L_i^{\mathrm{HHS}}(\Omega_i,\mathrm{DEM})$ at solid angle Ω_i is modeled as

$$L_i^{\mathrm{HHS}}(\Omega_i,\mathrm{DEM})=\Theta_sL_s\delta(\Omega_i-\Omega_s)+V_{di}L_d(\Omega_i)+V_{ci}L_c(\Omega_i) \tag{15}$$

where the binary quantity Θ_s is set to 1 or 0 as sunlight falls into Ω_{II} (unobstructed case, Figure 5a) or Ω_I

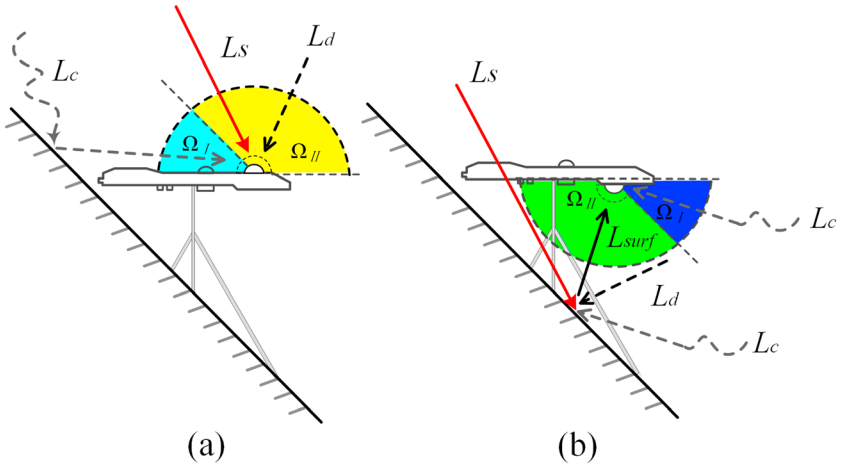

Figure 5. Radiative flux components of a horizontal radiometer over a sloped surface in the (a) incidence and (b) reflection. L_s, L_d, L_c, and L_{surf} are the direct, sky, adjacent slope-reflected, and target slope-reflected radiance, respectively.

(obstructed case, Figure 5a), respectively. V_{di} and V_{ci} are the binary coefficients that indicate whether sky radiance and slope-reflected radiance can be observed in Ω_i and adhere to the following relationship:

$$V_{di} = \begin{cases} 1 & \Omega_i \subseteq \Omega_{II} \\ 0 & \text{Others} \end{cases} \quad \text{and} \quad \frac{1}{\pi}\int_{2\pi(H)} V_{di}\cos\theta_i \mathrm{d}\Omega_i = V_d \tag{16}$$

$$V_{ci} = \begin{cases} 1 & \Omega_i \subseteq \Omega_{I} \\ 0 & \text{Others} \end{cases} \quad \text{and} \quad \frac{1}{\pi}\int_{2\pi(H)} V_{ci}\cos\theta_i \mathrm{d}\Omega_i = V_c \tag{17}$$

The downwelling irradiance $E_i^{\mathrm{HHS}}(\Omega_s, \mathrm{DEM})$ on a horizontal radiometer is

$$\begin{aligned} E_i^{\mathrm{HHS}}(\Omega_s, \mathrm{DEM}) &= \int_{2\pi(H)} L_i^{\mathrm{HHS}}(\Omega_i, \mathrm{DEM})\cos\theta_i \mathrm{d}\Omega_i \\ &= \int_{2\pi(H)} [\Theta_i L_s \delta(\Omega_i - \Omega_s) + V_{di} L_d(\Omega_i) + V_{ci} L_c(\Omega_i)]\cos\theta_i \mathrm{d}\Omega_i \end{aligned} \tag{18}$$

As the target-reflected irradiance $E_{\mathrm{surf}}^{\mathrm{HHS}}(\Omega_s, \mathrm{DEM})$ (Ω_{II}) occupies only a certain part of the radiometer FOV (Figure 5b), the adjacent slope-reflected irradiance E_c^{HHS} (Ω_I) without surface interaction is also included in the upward irradiance $E_r^{\mathrm{HHS}}(\Omega_s, \mathrm{DEM})$ reaching the downward pyranometer.

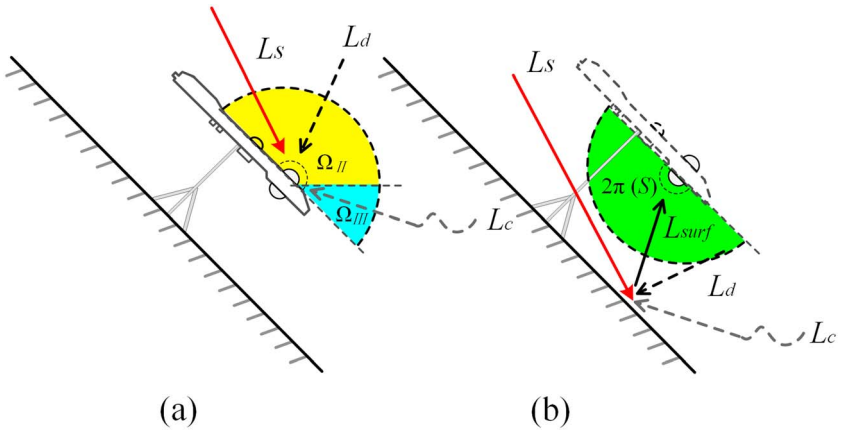

Figure 6. Radiative flux components of a slope-parallel positioned radiometer over a sloped surface in terms of the (a) incidence and (b) reflection. L_s, L_d, L_c, and L_{surf} are the direct, sky, adjacent slope-reflected, and target slope-reflected radiance, respectively.

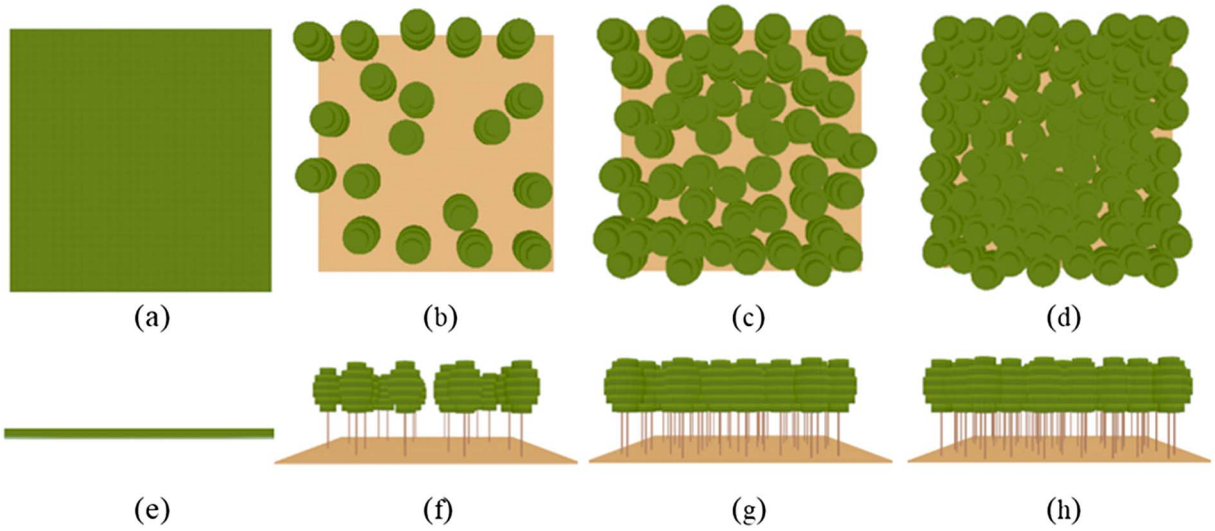

Figure 7. Nadir and perspective views of the 3-D DART simulations. (a, e) Continuous forest. (b, f) Sparse discontinuous forest. (c, g) Medium discontinuous forest. (d, h) Dense discontinuous forest.

$$E_r^{\mathrm{HHS}}(\Omega_s, \mathrm{DEM}) = E_{\mathrm{surf}}^{\mathrm{HHS}}(\Omega_s, \mathrm{DEM}) + E_c^{\mathrm{HHS}} \tag{19}$$

where $E_{\mathrm{surf}}^{\mathrm{HHS}}(\Omega_s, \mathrm{DEM})$ is modeled as

$$E_{\mathrm{surf}}^{\mathrm{HHS}}(\Omega_s, \mathrm{DEM}) = \frac{1}{\pi}\int_{2\pi(H)}\int_{2\pi(S)}\rho(\Omega_{ti}, \Omega_{tr})L_{\mathrm{surf}}(\Omega_{ti}, \Omega_{tr})\Theta_r \cos\theta_{ti}\mathrm{d}\Omega_{ti}\cos\theta_r\mathrm{d}\Omega_r \tag{20}$$

where Θ_r is the binary quantity, similar to Θ_s but in the reflecting geometry, and $L_{\mathrm{surf}}(\Omega_{ti}, \Omega_{tr})$ represents the radiance reflected from the target surface. The difference in the integral subscripts between the incidence and reflection occurs because the sloped surface receives irradiance from the upward sloped hemisphere, whereas the radiometer collects irradiance from the downward horizontal hemisphere. $L_{\mathrm{surf}}(\Omega_{ti}, \Omega_{tr})$ is modeled similar to the radiance in equation (15) but with local geometry:

$$L_{\mathrm{surf}}(\Omega_{ti}, \Omega_{tr}) = \Theta_i L_s\delta(\Omega_{ti} - \Omega_{ts}) + V_{di}L_d(\Omega_{ti}) + V_{ci}L_c(\Omega_{ti}) \tag{21}$$

E_c^{HHS} in equation (19) is equal to E_{tc} in equation (6). Thus, $E_r^{\mathrm{HHS}}(\Omega_s, \mathrm{DEM})$ is expanded as

$$E_{\mathrm{r}}^{\mathrm{HHS}}(\Omega_s, \mathrm{DEM}) = \frac{1}{\pi}\int_{2\pi(H)}\int_{2\pi(S)}\rho(\Omega_{ti}, \Omega_{tr})[\Theta_i L_s\delta(\Omega_{ti} - \Omega_{ts}) + V_{di}L_d(\Omega_{ti}) + V_{ci}L_c(\Omega_{ti})] \Theta_r \cos\theta_{ti}\mathrm{d}\Omega_{ti}\cos\theta_r\mathrm{d}\Omega_r + E_cV_c \tag{22}$$

Similar to HHFA, HHSA is modeled as the ratio of the hemispheric radiative flux reflected from a horizontal radiometer to incident radiative flux, which is horizontally positioned over a sloped surface.

$$\begin{aligned} HHSA = \alpha^{\mathrm{HHS}}(\Omega_s, \mathrm{DEM}) &= \frac{E_r^{\mathrm{HHS}}(\Omega_s, \mathrm{DEM})}{E_i^{\mathrm{HHS}}(\Omega_s, \mathrm{DEM})} \\ &= \frac{\frac{1}{\pi}\int_{2\pi(H)}\int_{2\pi(S)}\rho(\Omega_{ti}, \Omega_{tr})[\Theta_i L_s\delta(\Omega_{ti} - \Omega_{ts}) + V_{di}L_d(\Omega_{ti}) + V_{ci}L_c(\Omega_{ti})]\Theta_r \cos\theta_{ti}\mathrm{d}\Omega_{ti}\cos\theta_r\mathrm{d}\Omega_r}{\int_{2\pi(H)}[\Theta_i L_s\delta(\Omega_i - \Omega_s) + V_{di}L_d(\Omega_i) + V_{ci}L_c(\Omega_i)]\cos\theta_i\mathrm{d}\Omega_i} \\ &\quad + \frac{+E_cV_c}{\int_{2\pi(H)}[\Theta_i L_s\delta(\Omega_i - \Omega_s) + V_{di}L_d(\Omega_i) + V_{ci}L_c(\Omega_i)]\cos\theta_i\mathrm{d}\Omega_i} \end{aligned} \tag{23}$$

Compared with the direct solar radiation and diffuse skylight, the adjacent slope-reflected irradiance, including those that first arrive at the target surfaces and are then reflected back to the radiometer (Ω_{II} in Figure 5b) and those that directly enter the radiometer with surface interaction (Ω_I in Figure 5b), is relatively small

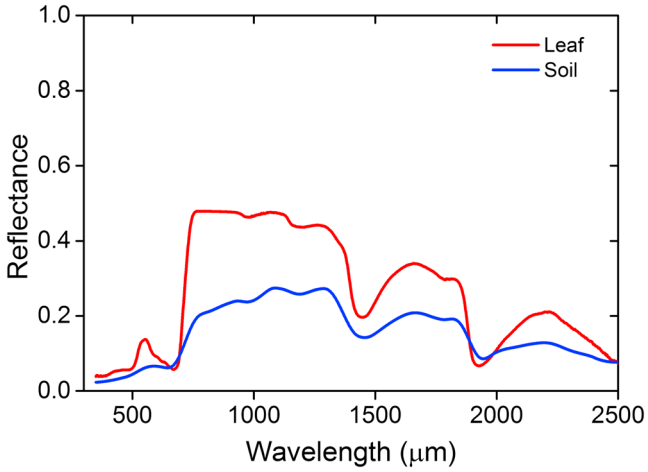

Figure 8. Component spectra selected from the Ground Object Spectral Library.

except over snow-covered surfaces or steep slopes. It is reasonable to neglect this radiative component in practical applications. Consequently, HHSA is quantified as

$$\mathrm{HHSA} = \alpha^{\mathrm{HHS}}(\Omega_s, \mathrm{DEM}) \approx \frac{\frac{1}{\pi}\int_{2\pi(H)}\int_{2\pi(S)}\rho(\Omega_{ti},\Omega_{tr})[\Theta_i L_s \delta(\Omega_{ti}-\Omega_{ts}) + V_{di}L_d(\Omega_{ti})]\Theta_r \cos\theta_{ti}\mathrm{d}\Omega_{ti}\cos\theta_r \mathrm{d}\Omega_r}{\int_{2\pi(H)}[\Theta_i L_s \delta(\Omega_i - \Omega_s) + V_{di}L_d(\Omega_i)]\cos\theta_i \mathrm{d}\Omega_i} \tag{24}$$

Furthermore, if the isotopic diffuse skylight is adopted, HHSA can be simplified to

$$\begin{aligned}
\mathrm{HHSA} = \alpha^{\mathrm{HHS}}(\Omega_s, \mathrm{DEM}) &\approx \frac{\Theta_s L_s \cos\theta_s \frac{\cos\theta_{ts}}{\cos\theta_s}\frac{1}{\pi}\int_{2\pi(H)}\rho(\Omega_{ti},\Omega_{tr})\Theta_r\cos\theta_r \mathrm{d}\Omega_r}{\Theta_s L_s\cos\theta_s + \pi L_d \frac{1}{\pi}\int_{2\pi(H)}V_{di}\cos\theta_i \mathrm{d}\Omega_i} \\
&+ \frac{\pi L_d \frac{1}{\pi^2}\int_{2\pi(H)}\int_{2\pi(S)}\rho(\Omega_{ti},\Omega_{tr})V_{di}\Theta_r\cos\theta_{ti}\mathrm{d}\Omega_{ti}\cos\theta_r\mathrm{d}\Omega_r}{\Theta_s L_s\cos\theta_s + \pi L_d \frac{1}{\pi}\int_{2\pi(H)}V_{di}\cos\theta_i\mathrm{d}\Omega_i} \\
&= \frac{\Theta_s E_s \frac{\cos\theta_{ts}}{\cos\theta_s}\frac{1}{\pi}\int_{\Omega_{II}}\rho(\Omega_{ti},\Omega_{tr})\cos\theta_r\mathrm{d}\Omega_r}{\Theta_s E_s + V_d E_d} + \frac{E_d\frac{1}{\pi^2}\int_{\Omega_{II}}\int_{\Omega_{II}}\rho(\Omega_{ti},\Omega_{tr})\cos\theta_{ti}\mathrm{d}\Omega_{ti}\cos\theta_r\mathrm{d}\Omega_r}{\Theta_s E_s + V_d E_d} \\
&= \frac{\Theta_s(1-f)\frac{\cos\theta_{ts}}{\cos\theta_s}\frac{1}{\pi}\int_{\Omega_{II}}\rho(\Omega_{ti},\Omega_{tr})\cos\theta_r\mathrm{d}\Omega_r}{\Theta_s(1-f)+fV_d} + \frac{f\frac{1}{\pi^2}\int_{\Omega_{II}}\int_{\Omega_{II}}\rho(\Omega_{ti},\Omega_{tr})\cos\theta_{ti}d\Omega_{ti}\cos\theta_r\mathrm{d}\Omega_r}{\Theta_s(1-f)+fV_d}
\end{aligned} \tag{25}$$

Equation (23) provides a physical expression of HHSA. Almost all current tower-based flux network observations over sloped surfaces belong to this case. Although the topographic effects are usually neglected in the operational airborne and satellite albedo retrieval algorithms, the derived products are similar to this quantity, as the reference plane in the reflectance characterization is horizontally positioned.

2.3.3. Inclined/Inclined Sloped Surface Albedo

As shown in CASE 5 (Table 1), when the instrument is positioned slope-parallel to simultaneously measure the downwelling and upwelling irradiances of a sloped surface (Figure 6), the radiometer-detected downward and upward irradiances conform with those impinging on and reflected by the target surface. Therefore, the measured albedo under this radiometer orientation is consistent with the true albedo quantifying the surface intrinsic reflection property. The downwelling irradiance $E_i^{\mathrm{IIS}}(\Omega_s, \mathrm{DEM})$ is calculated as

$$\begin{aligned}
E_i^{\mathrm{IIS}}(\Omega_s, \mathrm{DEM}) &= \int_{2\pi(S)} L_{\mathrm{surf}}(\Omega_{ti},\Omega_{tr})\cos\theta_{ti}\mathrm{d}\Omega_{ti} \\
&= \int_{2\pi(S)}[\Theta_i L_s\delta(\Omega_{ti}-\Omega_{ts}) + V_{di}L_d(\Omega_{ti}) + V_{ci}L_c(\Omega_{ti})]\cos\theta_{ti}\mathrm{d}\Omega_{ti}
\end{aligned} \tag{26}$$

The upwelling irradiance $E_r^{\mathrm{IIS}}(\Omega_s, \mathrm{DEM})$ is completely reflected from the target slope

$$E_r^{\mathrm{IIS}}(\Omega_s, \mathrm{DEM}) = \frac{1}{\pi}\int_{2\pi(S)}\int_{2\pi(S)}\rho(\Omega_{ti},\Omega_{tr})L_{\mathrm{surf}}(\Omega_{ti},\Omega_{tr})\cos\theta_{ti}\mathrm{d}\Omega_{ti}\cos\theta_{tr}\mathrm{d}\Omega_{tr} \tag{27}$$

IISA is modeled as the ratio of the hemispheric radiative flux reflected from a slope-parallel radiometer to incident radiative flux, which is positioned parallel to the target slope.

$$\mathrm{IISA} = \alpha^{\mathrm{IIS}}(\Omega_s, \mathrm{DEM}) = \frac{E_r^{\mathrm{IIS}}(\Omega_s, \mathrm{DEM})}{E_i^{\mathrm{IIS}}(\Omega_s, \mathrm{DEM})} = \frac{\frac{1}{\pi}\int_{2\pi(S)}\int_{2\pi(S)}\rho(\Omega_{ti}, \Omega_{tr})[\Theta_i L_s \delta(\Omega_{ti} - \Omega_{ts}) + V_{di}L_d(\Omega_{ti}) + V_{ci}L_c(\Omega_{ti})]\cos\theta_{ti}\mathrm{d}\Omega_{ti}\cos\theta_{tr}\mathrm{d}\Omega_{tr}}{\int_{2\pi(S)}[\Theta_i L_s \delta(\Omega_{ti} - \Omega_{ts}) + V_{di}L_d(\Omega_{ti}) + V_{ci}L_c(\Omega_{ti})]\cos\theta_{ti}\mathrm{d}\Omega_{ti}} \quad (28)$$

Similar to HHSA, if the adjacent slope-reflected irradiance is neglected, and the sky radiance is assumed to be isotropic, IISA can be simplified as

$$\mathrm{IISA} = \alpha^{\mathrm{IIS}}(\Omega_s, \mathrm{DEM}) \approx \frac{\Theta_s(1-f)\frac{\cos\theta_{ts}}{\cos\theta_s}\frac{1}{\pi}\int_{\Omega_{\mathrm{II}}+\Omega_{\mathrm{III}}}\rho(\Omega_{ts}, \Omega_{tr})\cos\theta_{tr}\mathrm{d}\Omega_{tr} + f\frac{1}{\pi^2}\int_{\Omega_{\mathrm{II}}+\Omega_{\mathrm{III}}}\int_{\Omega_{\mathrm{II}}}\rho(\Omega_{ti}, \Omega_{tr})\cos\theta_{ti}\mathrm{d}\Omega_{ti}\cos\theta_{tr}\mathrm{d}\Omega_{tr}}{\Theta_s(1-f)\frac{\cos\theta_{ts}}{\cos\theta_s} + fV_d} \quad (29)$$

3. Data Sets

3.1. Surface Albedo Simulated by 3-D DART Model

Although considerable efforts have been devoted to in situ albedo measurements over sloped surfaces in the last decades (Georg et al., 2016; Hoch & Whiteman, 2010; Mannstein, 1985; Matzinger et al., 2003; Serrano-Ortiz et al., 2016), there are still scarce data sets available to thoroughly explore topographic effects on surface albedo. Additionally, the airborne and satellite albedo products associated with topographic effects have not yet become accessible. Thus, a quantitative comparison between measured albedos with different radiometer orientations remains a great challenge. The 3-D ray tracing models offer an effective method to this issue, as they are accurate and efficient in the reproduction of near-realistic scenarios. The DART model is acknowledged as one of the most accurate 3-D ray tracing models evaluated by the four successive Radiation Transfer Model Intercomparison experiments (Gastellu-Etchegorry et al., 2015; Widlowski et al., 2007). DART provides an effective tool to generate and import varying landscape configurations, including land cover types, topographic characteristics, and atmospheric conditions.

DART provides both HHSA and IISA products. HHSA is simulated as the ratio of the upward scattered radiation to the total incident radiation on a horizontal projection above the scene. IISA is simulated by one minus the ratio of the radiation absorption to the total intercepted radiation through a global extrapolation method. This algorithm considers all scattered radiation (i.e., upward and downward) along the slope. To capture realistic plant cover, one homogeneous vegetation and three discontinuous forests (sparse, medium, and dense) were generated by DART (Figure 7). The crown counts of the discontinuous forests were 20, 50, and 80 with the same ellipsoid shapes (6 m along the vertical axis and 4 m along the horizontal axis, Table S1 in the supporting information). The leaf index area of continuous forest and the crown leaf index of discontinuous forest are 4.0. The leaf and background optical properties, as shown in Figure 8, were selected from the Chinese Ground Object Spectral Library (Zhang et al., 2017). The surface albedo in the visible (VIS, 400–700 nm), near-infrared (NIR, 700–2,500 nm), and shortwave (SW, 400–2,500 nm) broadbands were simulated. Seven slopes (0° to 60° in increments of 10°), 13 aspect orientations (0° to 360° in increments of 30°), and 7 SZAs (0° to 60° in increments of 10°) were input into DART. Additionally, in order to further investigate the difference in albedo diurnal cycle patterns under different vegetation structures and atmospheric conditions, sloped surface albedos of homogeneous continuous forest under 10 leaf area indexes (0.5 to 10 in increments of 0.5), 4 different atmospheric visibilities (clear-sky, 0.5 km, 5 km, and 23 km), and 6 standard atmospheric profiles (midlatitude summer, subarctic summer, tropical, midlatitude winter, subarctic winter, and 1976 U.S. standard) were simulated by DART.

3.2. In Situ Albedo Measurements

To further explore the differences in the albedo diurnal cycle patterns, in situ observations over four typical slopes were also used, where surface albedo was calculated from the observed downwelling and upwelling irradiance. Table 2 summaries the geographic and topographic characteristics of these four sites. Albedo measurements of a steep slope located at the Dayekou watershed (38°26′13″–38°34′26″N, 100°13′10″–

Table 2
Geographical and Topographical Information of In Situ Measurements

Sites	Surface type	Longitude/latitude	Altitude [a] m)	Slope/aspect [a]°)	Sensor height H/S[a] m)	Atmospheric condition	Observation period
DYK	Grassland	100°14′04″E/38°33′59″N	2,844	36/247	1.00/1.00	Clear	2016.9.14
ESM	Meadow	09°02′14″E/46°16′00″N	1,060	20/236	1.64[b] [a] 1.10[c])/1.20[b] [a] 1.20[c])	Clear, cloudy	1990.7.27–1990.10.11
ESR	Alpine	09°03′39″E/46°16′22″N	2,110	40/242	2.10[b] [a] 1.90[c])/2.15[b] [a] 1.90[c])	Clear, cloudy	1990.8.20–1990.10.9
CS-NF27	Alpine meadow	11°37′52″E/47°17′15″N	1,009	27/34	0.95[d]/1.95[d]	Clear, cloudy	2017.4.8–2017.4.14

[a]Indicate the horizontal and slope-parallel radiometers, respectively. [b]Sensor heights at ESM and ESR refer to Matzinger et al., 2003. [c]Four sensor heights are given at ESM and ESR since two Kipp & Zonen CM21[a]CM11) and two Kipp & Zonen CNR1 were used. 1.64 (1.10) represents that the heights of the incident and reflecting pyranometers are 1.64 and 1.10 m, respectively. [d]Sensor heights at CS-NF27 refer to Rotach et al., 2017.

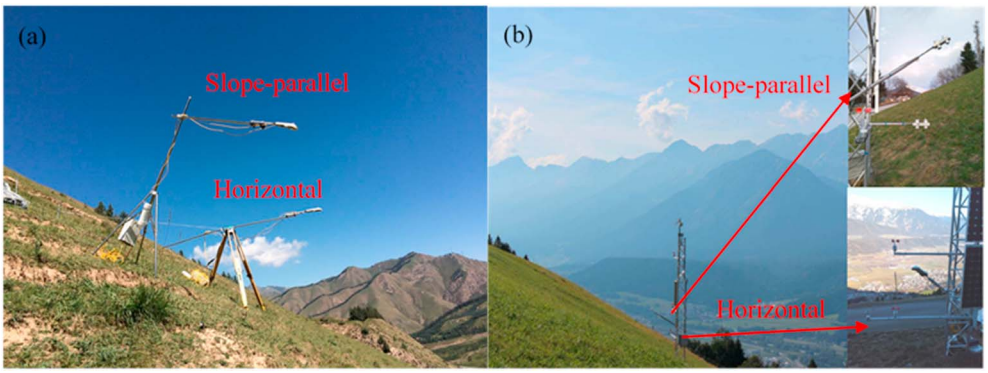

Figure 9. Horizontal and slope-parallel albedo measurements at (a) Dayekou and (b) CS-NF27.

100°18′52″E) in the Qilian Mountains of northwest China were carried out under a clear-sky day on 14 September 2016. The target slope was approximately 30 m × 20 m in size and was predominantly covered by grassland vegetation. Two horizontal and slope-parallel CNR4 net radiometers were mounted on the target surface to simultaneously measure the downwelling and upwelling SW fluxes (Figure 9a). The footprints of the pyranometers are resolved in the slope extent. The observations were taken from 9:30 to 17:30, and the signals were recorded at 1-min intervals by a data logger. The CNR4 radiometer was calibrated, and the cosine error was within 2‰ according to the manufacturer.

Surface radiation data collected in the Riviera Valley in southern Switzerland during the period of the Mesoscale Alpine Program Riviera subproject were selected (Matzinger et al., 2003). The valley width is approximately 1.5 km, with a mean slope of 30–35°. Various vegetation covers (e.g., forest, meadow, and agricultural land) are present in this valley owing to the varying solar radiation over different surface topographies. The radiation fluxes of seven sloped surfaces were measured, among which the upwelling and downwelling irradiances of the eastern slope with meadows (ESM) and the eastern slope with ridges (ESR) were simultaneously measured by two horizontal leveled Kipp & Zonen CM21 (CM11) and two slope-parallel leveled Kipp & Zonen CNR1, respectively. The measurements were conducted at half-hour intervals from 8:30 to 18:30 local standard time from 27 July to 11 October 1999 for ESM site and from 20 August to 9 October 1999 for ESR site. A description of these measurements was given in a previous study (Matzinger et al., 2003).

The Innsbruck Box (i-Box) project was conducted at the University of Innsbruck, which resides over Inn Valley in western Austria. It is an ongoing long-term experiment that aims to investigate the characteristics of turbulent structures and exchange processes for complex topography. The Inn Valley is a U-shaped valley in the Alps and has a valley floor width of approximately 2–3 km. The valley depth is approximately 1,700–2,100 m. The horizontal and slope-parallel radiation observations from a medium slope site (CS-NF27) from 8 to 14 April 2017 were used. The underlying surface is dominated by an Alpine meadow (Figure 9b). More details are provided in the previous literature (Rotach et al., 2017).

4. Results and Discussion

4.1. Topographic Effects on Surface Albedo

Figure 10 shows simulated black-sky broadband albedos over slopes facing toward the sun. Slopes are infinite so that the irradiances reflected from adjacent slopes are small. Similar surface albedo patterns associated with the slope are observed at different broadbands and decrease in the order of NIR, SW, and VIS broadbands, respectively. However, distinct patterns are caused by different radiometer orientations. The horizontal/horizontal flat surface black-sky albedo (α_{bs}^{HHF}) is independent of slope and has higher values at large SZAs than those at small SZAs due to multiple scattering effects (Liu et al., 2009). The horizontal/horizontal sloped surface black-sky albedo (α_{bs}^{HHS}) exhibits different patterns. When the SZA is 0°, α_{bs}^{HHS} decreases with the slope. When the SZA is 60°, as the slope increases from 0° to 40°, α_{bs}^{HHS} first increases to a local maximum then decreases as the slope further increases to 60° (Figures 9d–9f). As shown in equation (25), α_{bs}^{HHS} is the product of the cosine of the ratio of local and global SZAs and the integral of surface BRF within the effective

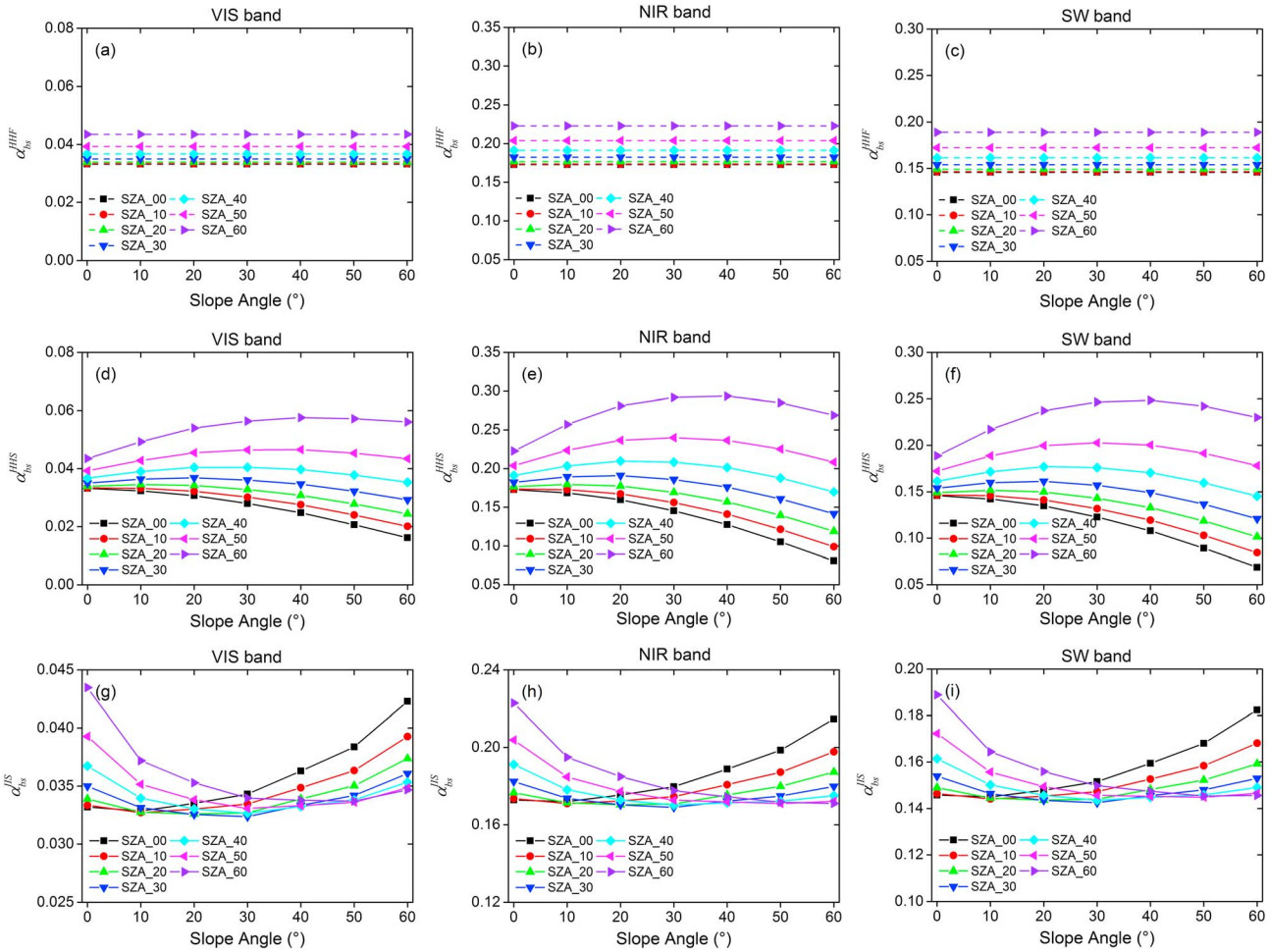

Figure 10. Effects of slope on (a–c) HHFA, (d–f) HHSA, and (g–i) IISA under clear-sky days in the VIS, NIR, and SW broadbands. Dashed curves indicate that HHFA is independent of slope. VIS = visible; NIR = near infrared; SW = shortwave; SZA = solar zenith angle; HHFA = horizontal/horizontal flat surface albedo; HHSA = horizontal/horizontal sloped surface albedo; IISA = inclined/inclined sloped surface albedo.

region (Ω_{II}) that receives the target surface reflected irradiance. For a horizontal radiometer over a sloped surface, the SZA remains constant. However, the cosine value of local SZA (Figure 10a) exhibits a decreasing trend under small SZAs and an increasing trend under large SZAs, and the effective exposure Ω_{II} (Figure 5b) decreases with slope. Consequently, α_{bs}^{HHS} shows two distinct patterns at small and large SZAs, respectively. Conversely, the inclined/inclined sloped surface black-sky albedos α_{bs}^{IIS} (Figures 10g–10i) over different slopes exhibit symmetric patterns at nearly 30° SZA, which is opposite to the cosine value of the local SZA in Figure 11a. This result is because α_{bs}^{IIS} characterizes the surface intrinsic reflection property that is related to incident solar zenith, as α_{bs}^{HHF} depends on the SZA over the horizontal surface. Although some different patterns occur at the α_{bs}^{IIS} of sparse discontinuous forest over a large slope due to the canopy gap effect (Webster et al., 2017), similar surface albedo patterns are observed for medium and dense forests (Figures S1–S3). The maximum absolute (relative) differences between α_{bs}^{HHS} and α_{bs}^{IIS} are up to 0.026 (61.8%), 0.134 (62.4%), and 0.114 (62.3%) in the VIS, NIR, and SW broadbands over a 60° sloped surface.

Figure 12 shows the effects of various aspects on the surface albedo of a 30° medium slope. α_{bs}^{HHF} is independent of the aspect. α_{bs}^{HHS} has typical concave-up shapes over different slope orientations, which is consistent with the cosine values of the local SZAs shown in Figure 11b. The missing value at 180° aspect in the curve of 60° SZA is attributed to the unexpected local SZA (90°). Conversely, as shown in Figures 12g–12i, α_{bs}^{IIS} exhibits dome-shaped patterns over varying aspects. These opposite patterns observed in α_{bs}^{HHS} and α_{bs}^{IIS} are because the incident irradiances collected by horizontal and slope-parallel radiometers are positively correlated with

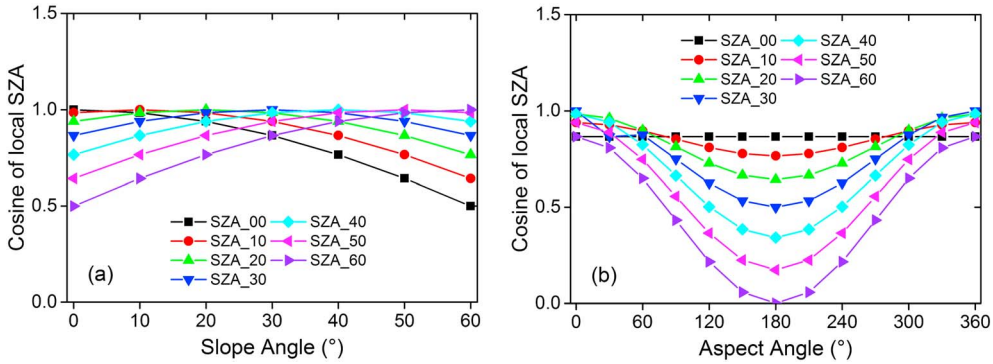

Figure 11. Cosine of local SZA on sloped surfaces with different (a) slopes and (b) aspects. SZA = solar zenith angle.

the cosine value of SZA and local SZA, respectively. The aspect induces similar effects on the surface albedo of discontinuous forests (Figures S4–S6).

4.2. Illumination Effects on Sloped Surface Albedos

Figure 13 shows the comparisons between black-sky albedos of sloped surfaces under three SZAs (0°, 30°, and 60°). Obvious discrepancies are revealed in the surface albedos of steep slopes at small and large

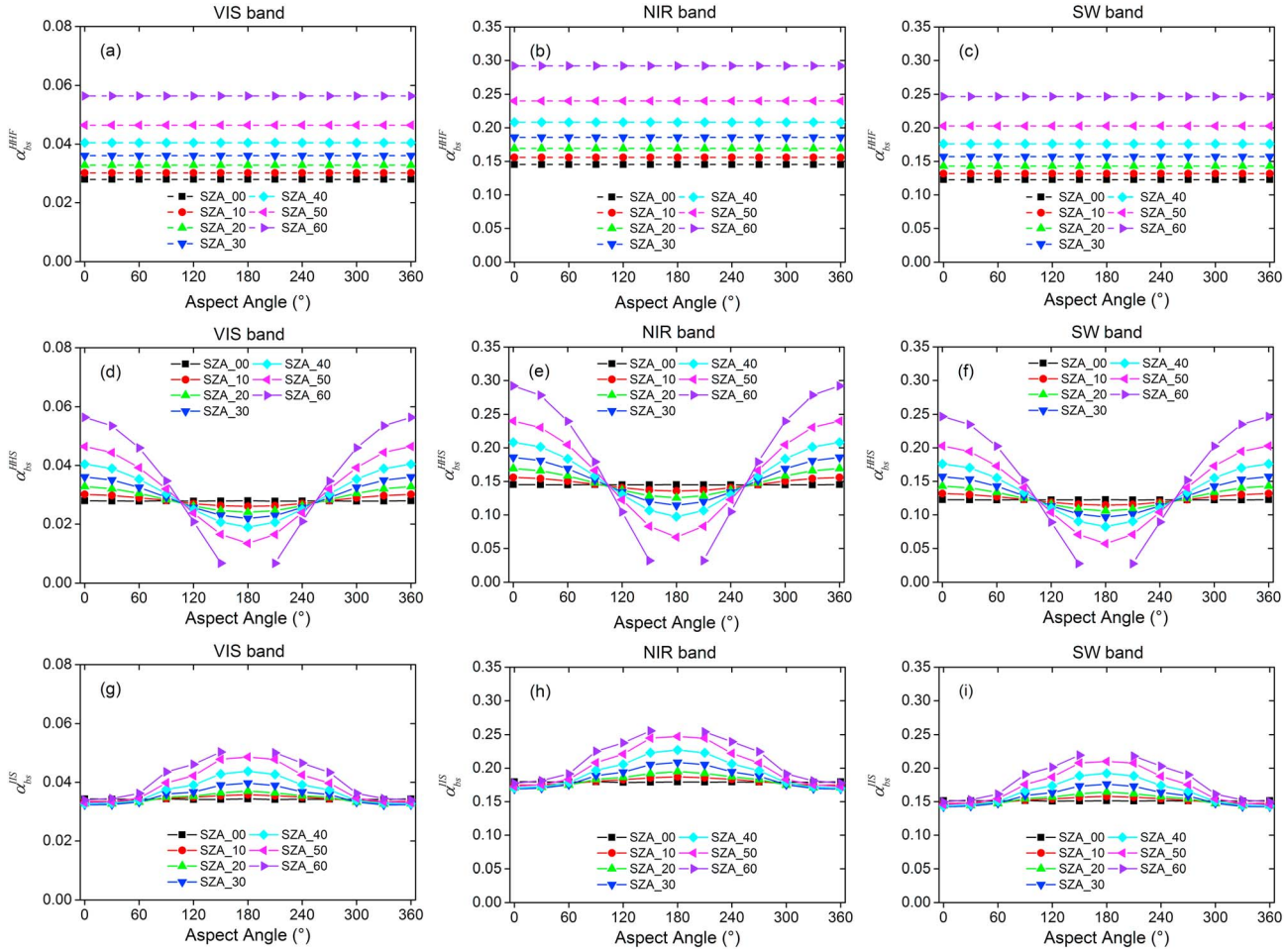

Figure 12. Effects of aspect on (a–c) HHFA, (d–f) HHSA, and (g–i) IISA under clear-sky days in the VIS, NIR, and SW broadbands. Dashed curves indicate that HHFA is independent of aspect. VIS = visible; NIR = near infrared; SW = shortwave; SZA = solar zenith angle; HHFA = horizontal/horizontal flat surface albedo; HHSA = horizontal/horizontal sloped surface albedo; IISA = inclined/inclined sloped surface albedo.

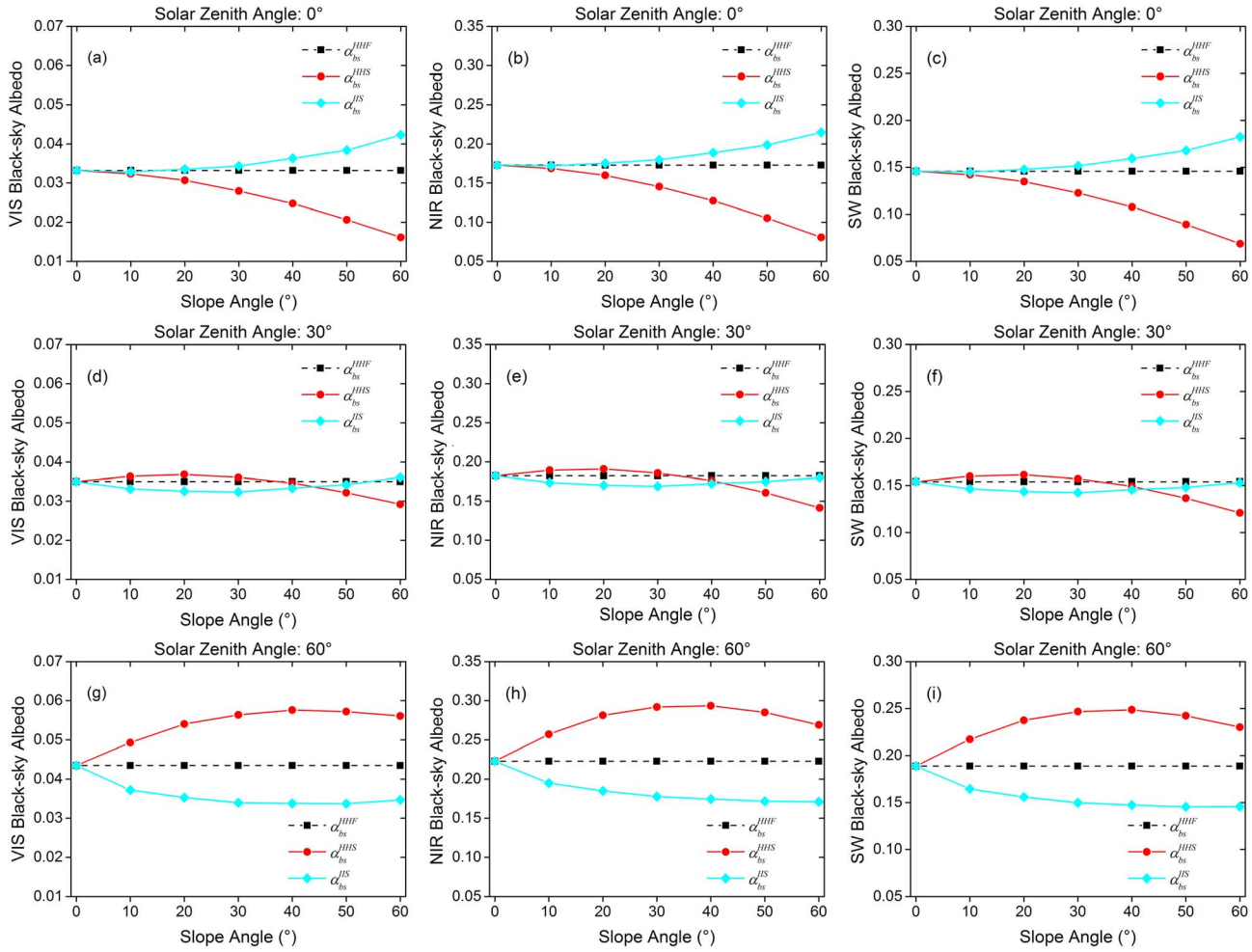

Figure 13. Effects of slope on black-sky albedos for (a–c) 0°, (d–f) 30°, and (g–i) 60° solar zenith angles. VIS = visible; NIR = near infrared; SW = shortwave.

SZAs. When the Sun is at nadir, the albedos decreased in the order of α_{bs}^{IIS}, α_{bs}^{HHF}, and α_{bs}^{HHS}, while for a 60° SZA, the albedos decreased in the order of α_{bs}^{HHS}, α_{bs}^{HHF}, and α_{bs}^{IIS}. Effects of SZA on black-sky albedos for the SW broadband are illustrated in Figure 14. Albedos have a typical concave-up shape as the SZA increases because solar radiation penetrates into deeper vegetation at smaller SZAs, which are more likely to be captured and absorbed by the vegetation. (Liu et al., 2009). As the slope increases, the rate of increase in α_{bs}^{HHS} increases, while α_{bs}^{IIS} decreases, creating a concave-down shape. The result is because that α_{bs}^{HHS} is determined by $\frac{\cos\theta_{ts}}{\cos\theta_s}$ and the integral of surface BRF within Ω_{II} in equation (25), while α_{bs}^{IIS} depends on the integral of surface BRF within 2π(S) in equation (29).

In contrast to black-sky albedo, where sunlight hits the surface at a specific solar geometry, the sky radiance occupies the whole hemisphere for white-sky albedo. However, due to the topographic obstruction, the effective FOVs of horizontal and slope-parallel radiometers (Figure 5a and 6a) are reduced to Ω_{II}, which leads to an identical incident diffuse irradiance arriving at the target slope when the diffuse radiance is isotropic. Therefore, the differences in white-sky albedo are caused by the effective FOVs in the reflection that collect surface reflected irradiance. As shown in equation (25) and Figure 5b, Ω_{II} in the reflection of the horizontal/horizontal sloped surface white-sky albedo (α_{ws}^{HHS}) decreases with the slope angle. Therefore, α_{ws}^{HHS} decrease with the slope (Figure 15). The effective exposure of a slope-parallel radiometer is close to the downward sloped hemisphere, and the inclined/inclined sloped white-sky albedo (α_{ws}^{IIS}) is relatively independent of the slope. α_{ws}^{IIS} is close to the HHFA (α_{ws}^{HHF}) although slight smaller values are revealed. Similar patterns are observed for the discontinuous forest canopy (Figure S7). The effects of diffuse skylight on surface

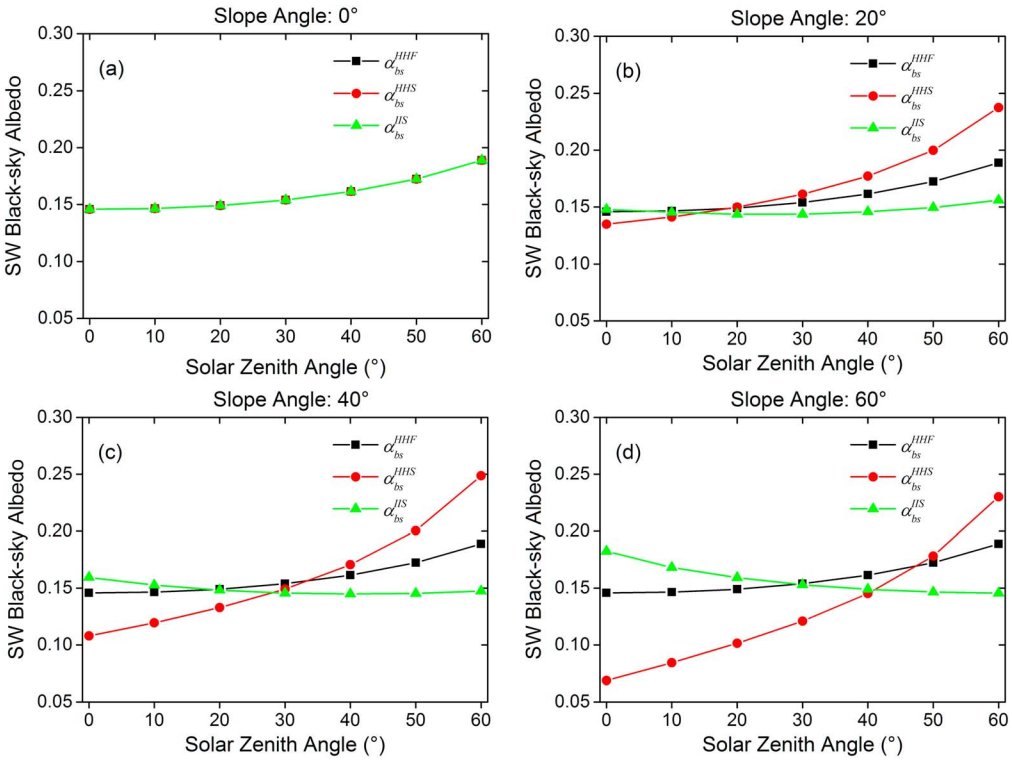

Figure 14. Effects of solar zenith angle on black-sky albedos for (a) 0°, (b) 20°, (c) 40°, and (d) 60° slopes. SW = shortwave.

albedos are illustrated in Figure 16. Given a slope, as the diffuse skylight proportion increases, the shape of the blue-sky albedo curve becomes smoother.

4.3. Comparison Between Horizontal and Slope-Parallel Measured Albedos

The differences in the daily patterns of horizontal and slope-parallel albedo will give rise to differences in the surface energy budget. For example, Figure 17 displays the daily incoming and outgoing irradiances simultaneously observed by a horizontal and a slope-parallel radiometer at CS-NF27 under a clear-sky day on 9 April 2017. The incoming and outgoing irradiances of a horizontal radiometer are symmetric along local solar noon. However, the peak of incoming irradiance collected by a slope-parallel radiometer is approximately 2 hr ahead of local solar noon due to the northwestern orientation with an advanced local SZA (Figure 18d). Owing to the differences in the measured surface albedo (Figure 18d), the peak of outgoing irradiance of a slope-parallel radiometer is delayed approximately 1 hr compared with that of a horizontal radiometer. Therefore, it is essential to investigate the differences between and drivers of α^{HHS} and α^{IIS}.

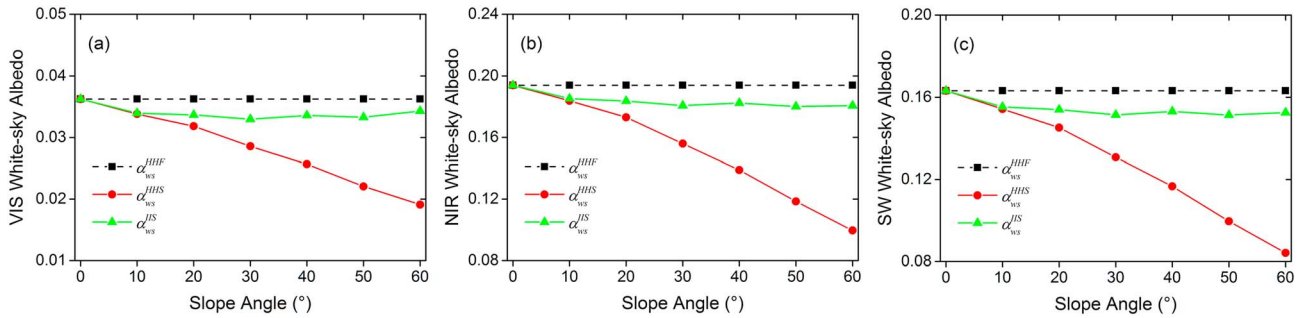

Figure 15. (a–c) Effects of slope on surface white-sky albedos. VIS = visible; NIR = near infrared; SW = shortwave.

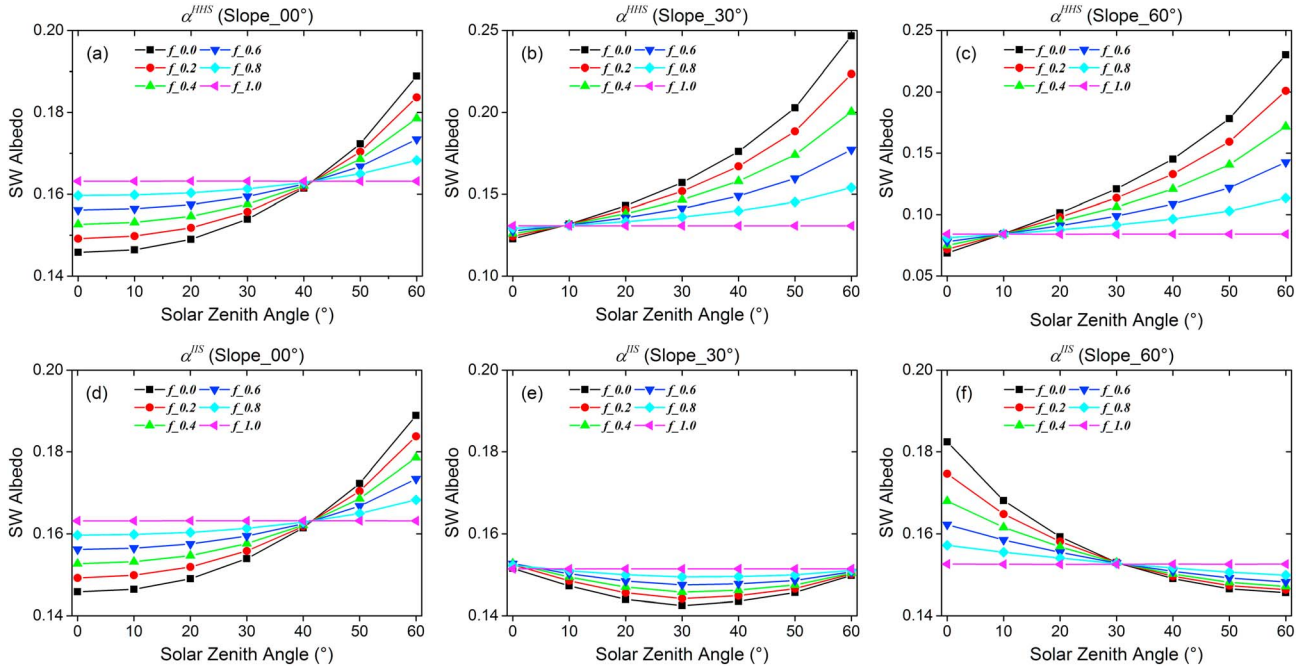

Figure 16. Effects of diffuse skylight on (a–c) horizontal and (d–f) slope-parallel blue-sky albedos. SW = shortwave.

The comparisons between observed albedo diurnal courses under clear-sky conditions at four slopes are represented in Figure 18, where the diurnal changes in global and local SZAs are also illustrated. The DART simulations over the same sites during the same observation time are compared (Figure S8). It is noted that the blank areas at DYK in 12:00–12:30 and 16:30–17:00 local standard time are due to missing records. The DART simulations are highly correlated with the in situ measurements (coefficient of determinations [R^2] of $\frac{\alpha_{bs}^{IIS}}{\alpha_{bs}^{HHS}}$ at DYK, ESR, ESM, and CS-NF27 are 0.99, 0.94, 0.96, and 0.90, respectively. $p < 0.05$, Figure S9), indicating that DART is able to accurately capture surface albedo patterns.

As shown in Figure 18, due to the similar southeastern orientations, α^{HHS} of DYK, ESM, and ESR have similar patterns that increase monotonically with local standard time, while α^{IIS} decreases with local standard time. In contrast, α^{HHS} and α^{IIS} of CS-NF27 have inversed trends. The daily patterns of α^{HHS} are explained by $\frac{\cos\theta_{ts}}{\cos\theta_s}$ in equation (25), as f is close to 0, and the effective FOV Ω_{II} remains constant in this case. This conclusion is quite different from a previous study, which attributes the increased α^{HHS} to an increase in anisotropic diffuse irradiance in the afternoon and a predominantly forward surface reflectance (Matzinger et al., 2003). As shown in equation (29), as f approaches to zero, α^{IIS} is determined by the integral of surface BRF within $2\pi(S)$. Thus, the decreased α^{IIS} is due to the daily variation in local SZA and surface BRF. Although the illuminations are close to those for a clear sky, a diffuse sky occurs between astronomical and local sunrise, during which time the signal-to-noise ratio of the pyranometer is low. Thus, smaller surface albedos are observed at ESM before 08:30 local standard time and at ESR before 09:30 local standard time.

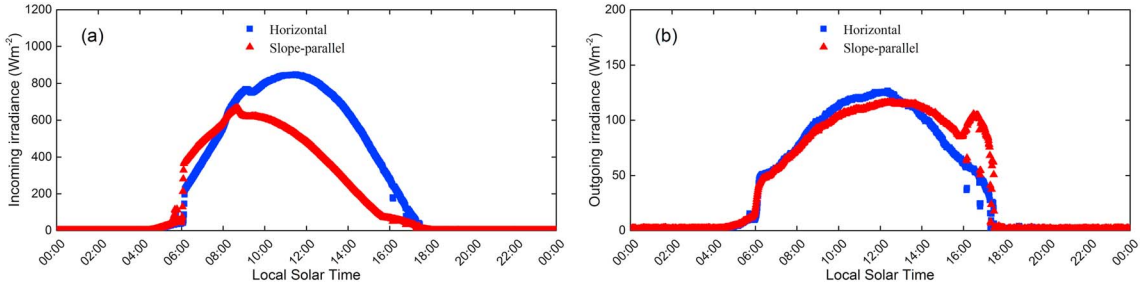

Figure 17. Diurnal cycles of (a) incoming and (b) outgoing irradiance over horizontal and slope-parallel radiometers at CS-NF27 under a clear-sky day on 9 April 2017.

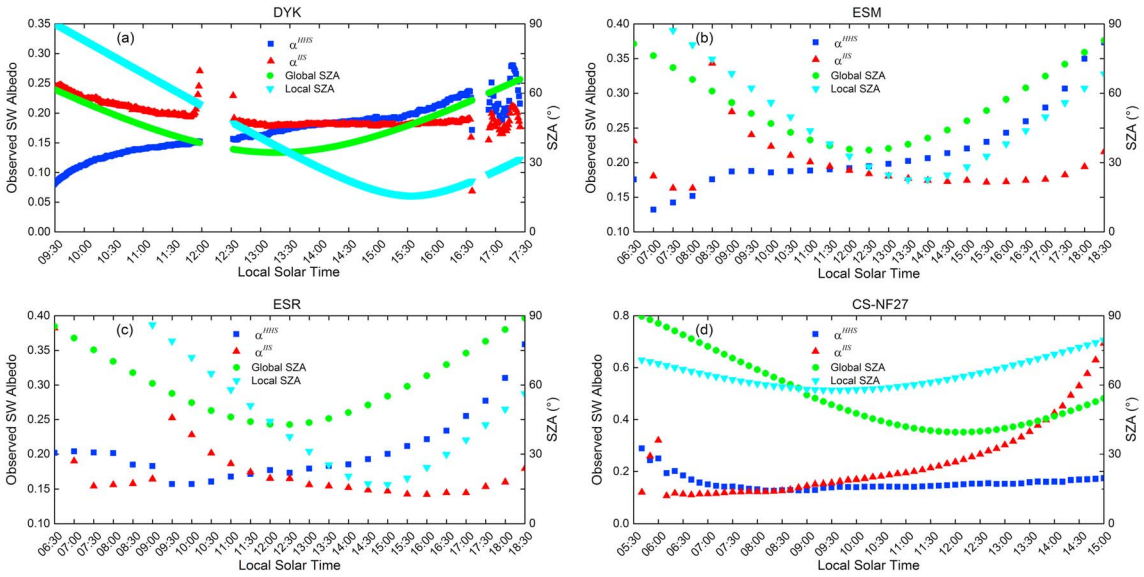

Figure 18. Comparison between observed diurnal courses of horizontal and slope-parallel albedos at (a) DYK on 14 September 2016, (b) ESM on 25 August 1999, (c) ESR on 14 September 1999, and (d) CS-NF27 on 9 April 2017. ESM = eastern slope with meadows; ESR = eastern slope with ridges; SW = shortwave; SZA = solar zenith angle.

Considering the distinct difference between α^{HHS} and α^{IIS}, a transformation relationship between these two albedos is important for determining the surface energy budget with the intrinsic surface albedo (Jonsell et al., 2003; Sicart et al., 2001; Weiser et al., 2016). For a clear-sky day, a cosine equation ($\frac{\cos\theta_{ts}}{\cos\theta_s}$) is frequently used to correct α^{HHS} to α^{IIS}. Based on this method, the interaction position where α^{HHS} is equal to α^{IIS} should be the same as the interaction position where $cos\theta_s$ is equal to $\cos\theta_{ts}$. However, an approximately half-hour lag is observed between these two interaction positions over the steep slopes of DYK (Figure 18a) and ESR (Figure 18c). These biases result from different effective exposures to the sloped surface in the reflection (equations (25) and (29)). As shown in Figures 5b and 6b, the effective FOV of a horizontally positioned radiometer (Ω_{II}) is smaller than that of a slope-parallel radiometer ($\Omega_{II} + \Omega_{III}$). Additionally, as slope DYK and ESR are far from adjacent slope, the reflected irradiance is smaller within Ω_I in α^{HHS} (Figure 5b) compared with α^{IIS}. Thus, the lag offsets at DYK and ESR are larger than that at ESM because of the larger slope. The difference between α^{HHS} and α^{IIS} is larger in the early morning and later afternoon than that at local solar noon. This result is explained by the difference in $\cos\theta_s$ and $\cos\theta_{ts}$ and the measurement error due to low-energy availability.

To further investigate topographic effects on albedo daily patterns, surface albedos over varying slopes and orientations were simulated under a clear-sky day using the same solar geometry from DYK on 14 September 2016. $\frac{\alpha^{IIS}}{\alpha^{HHS}}$ and $\frac{\cos\theta_{ts}}{\cos\theta_s}$ over a medium slope (20°) and a steep (40°) slope are shown in Figure 19. When the slopes are north or south facing, $\frac{\alpha^{IIS}}{\alpha^{HHS}}$ seems to be steady during the daytime period due to a stable $\frac{\cos\theta_{ts}}{\cos\theta_s}$. As the slope

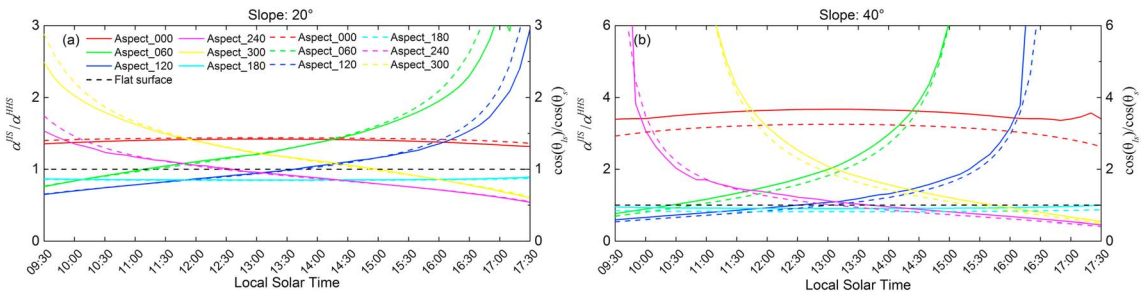

Figure 19. Simulated diurnal courses of albedo ratio for (a) 20° and (b) 40° slopes. Bold curve represents the albedo ratio. Dashed curve represents the cosine ratio of local and global solar zenith angles. HHS = horizontal/horizontal sloped surface; IIS = inclined/inclined sloped surface.

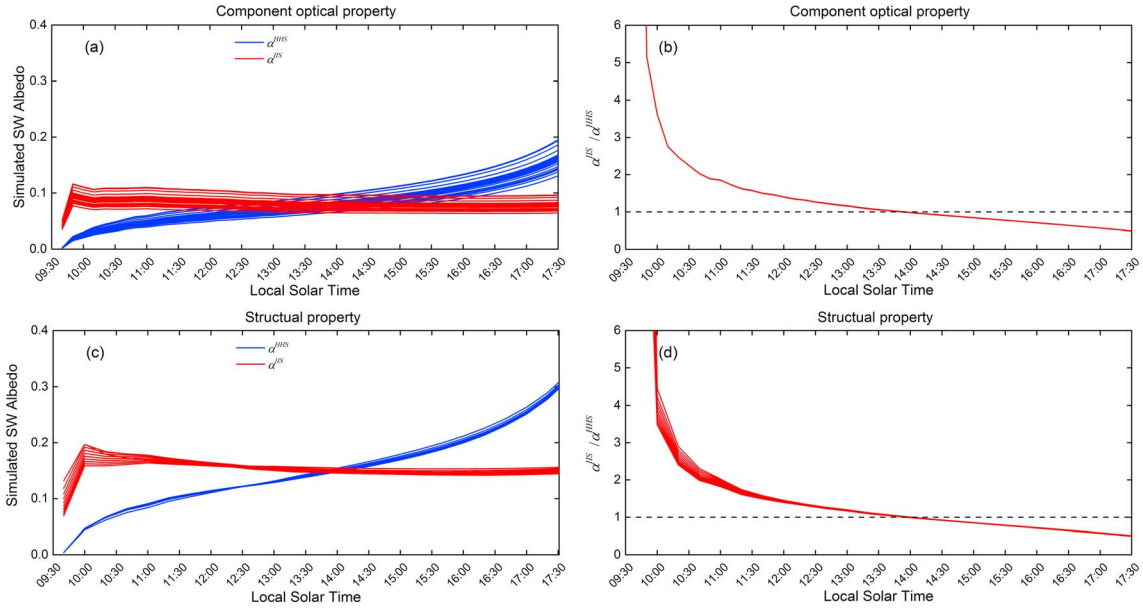

Figure 20. Effects of (a and b) optical and (c and d) structural properties on the diurnal courses in albedo. SW = shortwave.

moves toward east or west, $\frac{\alpha^{IIS}}{\alpha^{HHS}}$ displays varying patterns, which increases monotonously with local standard time at the western slopes but decreases at the eastern slopes. The interaction position between $\frac{\alpha^{IIS}}{\alpha^{HHS}}$ with dashed line $y = 1$ indicates the situation where α^{IIS} is equal to α^{HHS}. The aspect determines whether the albedo interaction position is early or delayed compared to the local solar noon. For example, for a medium slope with a 60° aspect, the interaction point is located at 11:20 local standard time, approximately 2 hr ahead of the local solar noon (13:20 local standard time). An additional hour ahead of the local solar noon is observed for steeper slopes with the same aspect (Figure 19b). It is interesting to find that $\frac{\alpha^{IIS}}{\alpha^{HHS}}$ is not exactly equal to $\frac{\cos\theta_{ts}}{\cos\theta_s}$, as reported in a previous study (Weiser et al., 2016), especially at a large slope or in the early morning and late afternoon. These results can be explained by the different radiometer exposures and the low cosine response of the radiometer at large SZAs (Dirmhirn & Eaton, 1975).

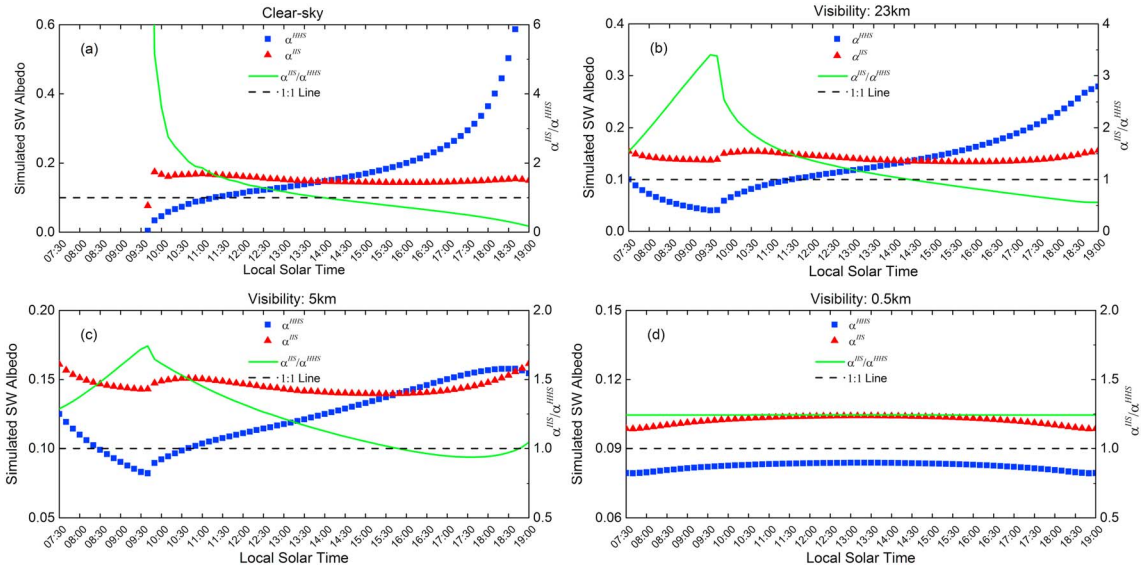

Figure 21. Simulated albedo diurnal changes at DYK under (a) clear-sky, (b) partly cloudy, (c) cloudy, and (d) overcast conditions. SW = shortwave.

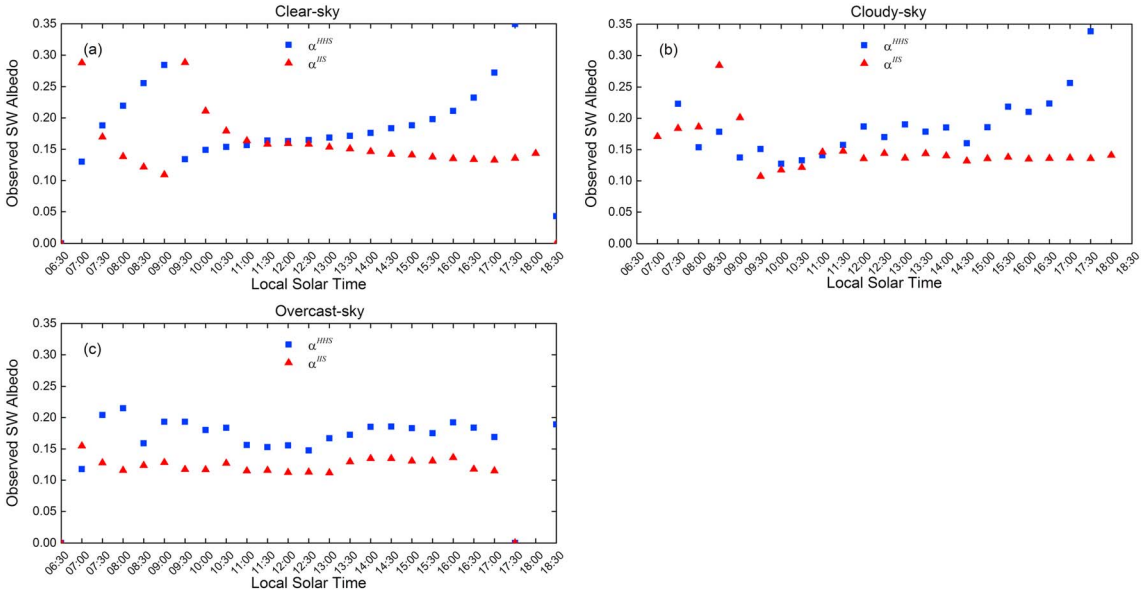

Figure 22. Observed albedo diurnal changes at ESR under (a) clear-sky, (b) cloudy, and (c) overcast conditions. SW = shortwave.

The effects of component structural and optical properties on diurnal courses in surface albedos are shown in Figure 20, where a total of 30 soil spectra was selected from the Ground Object Spectral Library, and leaf area index ranges from 0.5 to 5.0 with an increment of 0.5. Although different component optical properties lead to varying surface albedos, the daily albedo have relatively stable patterns (Figure 20a and 20b). Particularly, $\frac{\alpha^{IIS}}{\alpha^{HHS}}$ appears to be independent of component spectral properties. This reason explains the similar albedo diurnal courses between the in situ measurements and DART simulations (Figures 18 and S8), even though leaf and soil spectra were selected from the spectral library. Similarly, as shown in Figures 20c and 20d, the structural property also presents a small effect on albedo diurnal cycle. These findings reveal that the transformation between α_{bs}^{HHS} and α_{bs}^{IIS} is independent of the optical and structural parameters.

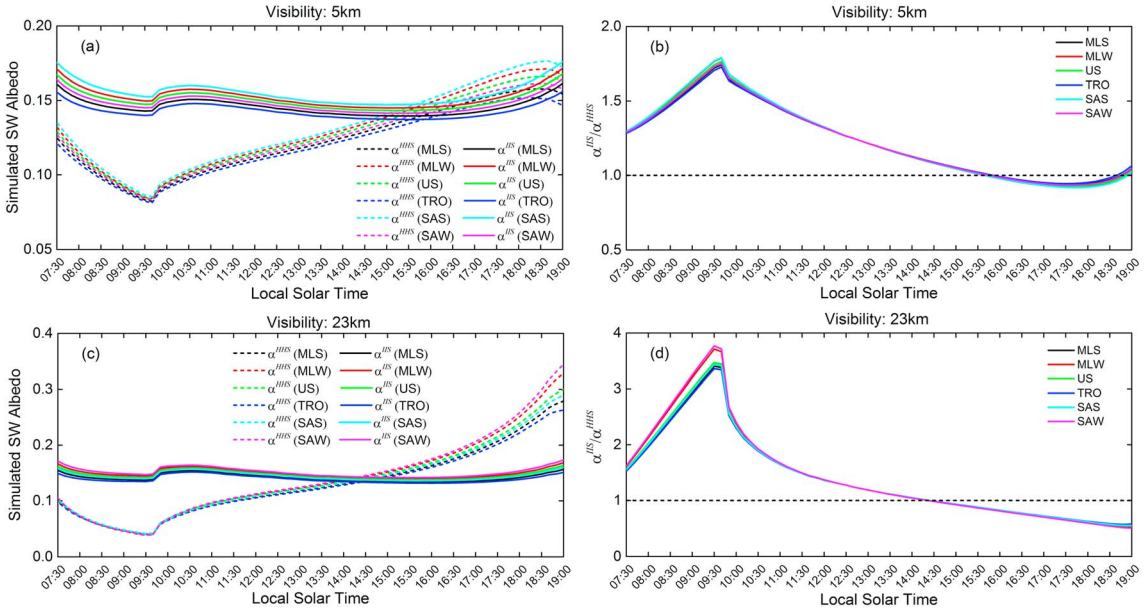

Figure 23. Simulated albedo diurnal changes at DYK with varying atmospheric profiles under (a and b) 5-km and (c and d) 23-km atmospheric visibilities. SW = shortwave; MLS = midlatitude summer MLW = midlatitude winter; US = U.S. standard; TRO = tropical; SAS = subarctic summer; SAW = subarctic winter.

Diffuse skylight is another crucial factor for surface albedo (Román et al., 2010). Albedo diurnal changes at DYK under four atmospheric visibilities (clear sky, 23, 5, and 0.5 km) were simulated with the mid-latitude summer atmospheric profile and rural aerosol model. As shown in Figure 21a, when only direct solar radiation exists, albedo occurs between local sunrise and local sunset, and α^{HHS} and α^{IIS} match at approximately 14:00 local standard time. On a partly cloudy day (Figure 21b), albedo begins near astronomical sunrise and continues until astronomical sunset. In the morning hours between astronomical and local sunrise, albedo is attributed to the diffuse skylight contribution. Compared with clear-sky days, α^{IIS} and α^{HHS} interaction location is delayed by approximately a half hour at 14:30. As the atmospheric visibility reduces to 5 km, the moment of albedo matching is further delayed to 15:50 local standard time. When the sky is completely overcast with diffuse skylight, both α^{IIS} and α^{HHS} exhibit stable and similar diurnal changes without SZA dependence. This systematic difference is explained by the different effective exposures in the reflection. Similar daily albedo patterns are observed at ESR under clear-sky, cloudy, and overcast conditions (Figure 22). The albedo patterns were similar under different atmospheric profiles (Figure 23). However, the patterns of albedo ratios show slight dependence on atmospheric profiles. This result is because similar diffuse skylight proportions are shared by a specific atmospheric visibility.

5. Conclusions

Over the past few decades, global satellite albedo products with varying spatial resolutions and temporal frequencies have become available from the remote sensing community. However, surface albedo retrieval algorithms accounting for topographic effects are still limited and are popular topics in ongoing studies. In situ albedo measurements are critical for albedo product validation, algorithm calibration and improvement, and surface energy budget estimation. However, efforts to improve albedo measurements face great challenges because the appropriate interpretations of surface albedo are still lacking. This study characterized and analyzed two commonly used sloped surface albedos associated with different radiometer orientations. HHSA is measured by a horizontal radiometer and is usually used in the tower-based flux network observations and current remote sensing albedo retrieval algorithms. IISA is measured by a slope-parallel radiometer and conforms with surface intrinsic reflectivity since the incidence and reflection are consistent with those of the target surface.

From 3-D DART simulations with continuous and discontinuous forest canopies, surface broadband albedos show similar patterns over different slopes and aspects and decreased in the order of NIR, SW, and VIS broadbands. For the varying slopes, aspects, and illumination conditions, HHSA and IISA exhibit distinct patterns because their primary topographic factors are different. HHSA relies on local and global SZAs and sky-view and terrain-view factors. IISA relies on the local SZA and sky-view and terrain-view factors. The difference between HHSA and IISA lies on the effective FOVs, which lead to different irradiances in the incident and reflected geometry. For the incident irradiance, HHSA horizontally collects direct solar radiation, diffuse skylight, and irradiance reflected from the slope and adjacent slopes, while slope-parallel radiometer observes direct solar radiation, diffuse skylight, and irradiance reflected from adjacent slopes. For the reflected irradiance, HHSA includes two components, surface reflected irradiance, and adjacent slope-reflected irradiance, while IISA only observes surface reflected irradiance. For a 60° sloped surface, the maximum absolute (relative) biases between HHSA and IISA reached up to 0.026 (61.8%), 0.134 (62.4%), and 0.114 (62.3%) in the VIS, NIR, and SW broadbands, respectively, exceeding the absolute accuracy (0.02–0.05) required by climate models (Sellers et al., 1995). Compared with the continuous canopy, the albedo of discontinuous forest is more complicated due to its horizontal and vertical structural heterogeneity. In particular, the effects of canopy gap might give rise to some uncertainties in surface albedo estimation (Figure S1).

Changing albedo daily patterns are observed due to the different responses of HHSA and IISA to the topography, illumination geometry, and atmospheric conditions. For the southeastern slopes DYK, ESR, and ESM, HHSA increases, while IISA decreases with the local standard time. In contrast, HHSA and IISA of northwestern slope CS-NF27 exhibit the opposite daily trend. These difference cause different patterns in the outgoing SW irradiance collected by the horizontal and slope-parallel radiometers (Figures 17 and S10). For example, the slope-parallel measured outgoing irradiance peak at CS-NF27 lags behind that measured horizontally, and a

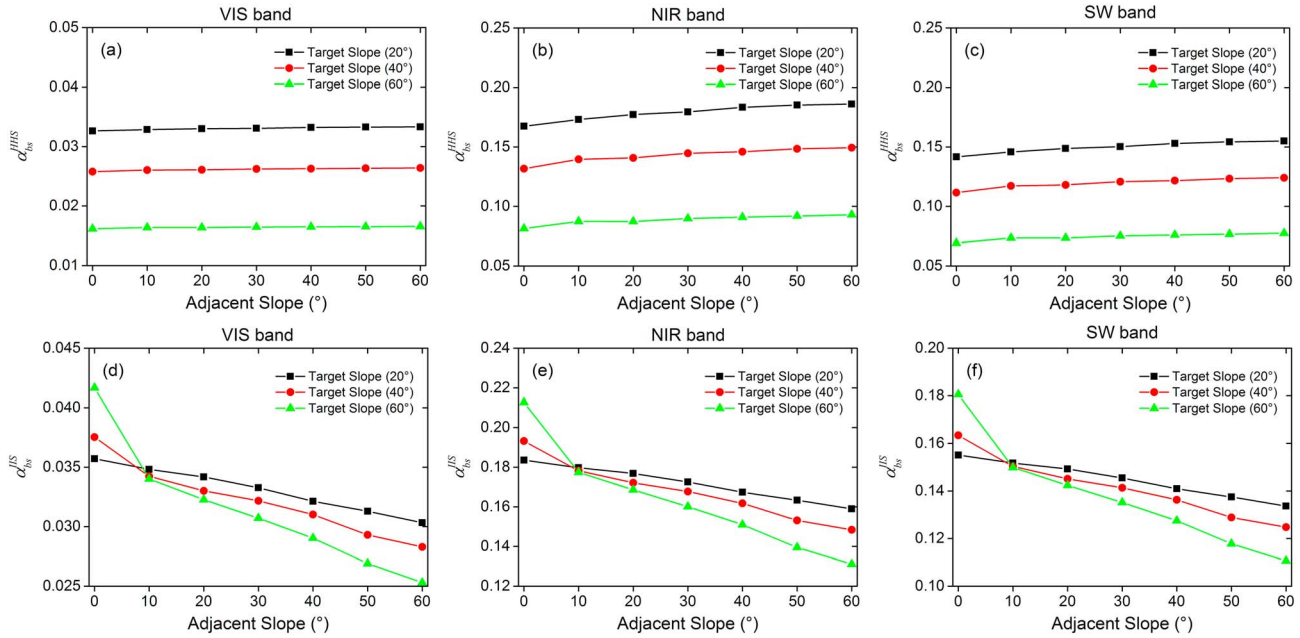

Figure 24. Effects of adjacent slope-reflected irradiance on α_{bs}^{HHS} and α_{bs}^{IIS} at nadir illumination. VIS = visible; NIR = near infrared; SW = shortwave.

maximum absolute bias of 38 W/m^2 occurs at DYK. It should be emphasized that IISA is suggested to be adopted in the surface energy budget, as it is physically consistent with the surface intrinsic reflectivity (Matzinger et al., 2003; Weiser et al., 2016). It is also recommended as the standardized albedo in the remote sensing retrievals and in situ measurement. However, the slope-parallel placements are usually restricted at a local scale due to the safety and stability requirements of the radiometer. For example, a horizontal radiometer instead of slope-parallel radiometer is used in the tower-based flux network, especially when measuring the albedo of tall forest canopies or slopes with several resolved subslopes. In this case, the transformation between HHSA and IISA is suggested. Previous studies reveal that a Lambertian correction is a good solution for clear-sky days (Joerg et al., 2015). However, our result shows that this strategy might cause some biases over those steep slopes that are far away from surrounding mountainous since the FOV effect of a horizontal radiometer in the reflection is smaller than that of a slope-parallel radiometer. Due to the stable albedo transformation relationship and high signal-to-noise ratio of pyranometer at solar noon, the ground measurements are suggested to be carried out near local solar noon to evaluate remote sensing albedo products (Sicart et al., 2001). Additionally, the measurements are usually collected in remote areas, creating a great challenge for regular maintenance. For example, the geometry of a radiometer over glaciers or seasonal snow fields may change due to the slope movements (e.g., landslide, snow melting, refreezing, and riming). The general method proposed in this paper to correct broadband albedo affected by unknown slope and sensor tilts is promising (Weiser et al., 2016).

When diffuse irradiance exists, surface albedo and its daily variations are more complicated. In this case, the full albedo expressions in equations (23) and (28) are suggested where both the diffuse skylight and adjacent slope-reflected irradiance are considered (Figures S11 and S12). In our simulations, the adjacent slope-reflected irradiance is neglected. Thus, three slopes (20°, 40°, and 60°, Figure S13) with four adjacent slopes (0°, 20°, 40°, and 60°) were designed to investigate slope-reflected irradiance on black-sky and white-sky surface albedos. The results are shown in Figures 24 and 25. HHSA seems unaffected by the adjacent slope at the VIS broadband (a maximum relative bias of 2.75%) but increases with the slope of the adjacent terrain at the NIR and SW broadbands with maximum absolute (relative) biases of 0.015 (16.0%) and 0.010 (13.3%), respectively. These results can be explained by a decreased direct solar radiation or sky radiance within Ω_{II_2} (Figure S11a) possibly being comprised by the increased slope-reflected irradiance within Ω_I and Ω_{II} in the reflection (Figure S11b and equation (23)). Conversely, IISA decreases with the slope of adjacent terrain since the increased slope-reflected irradiance is smaller than the reduced direct solar radiation or sky radiance (Figure S12). The maximum absolute (relative) bias values of a 60° slope are up to 0.016 (39.3%), 0.082

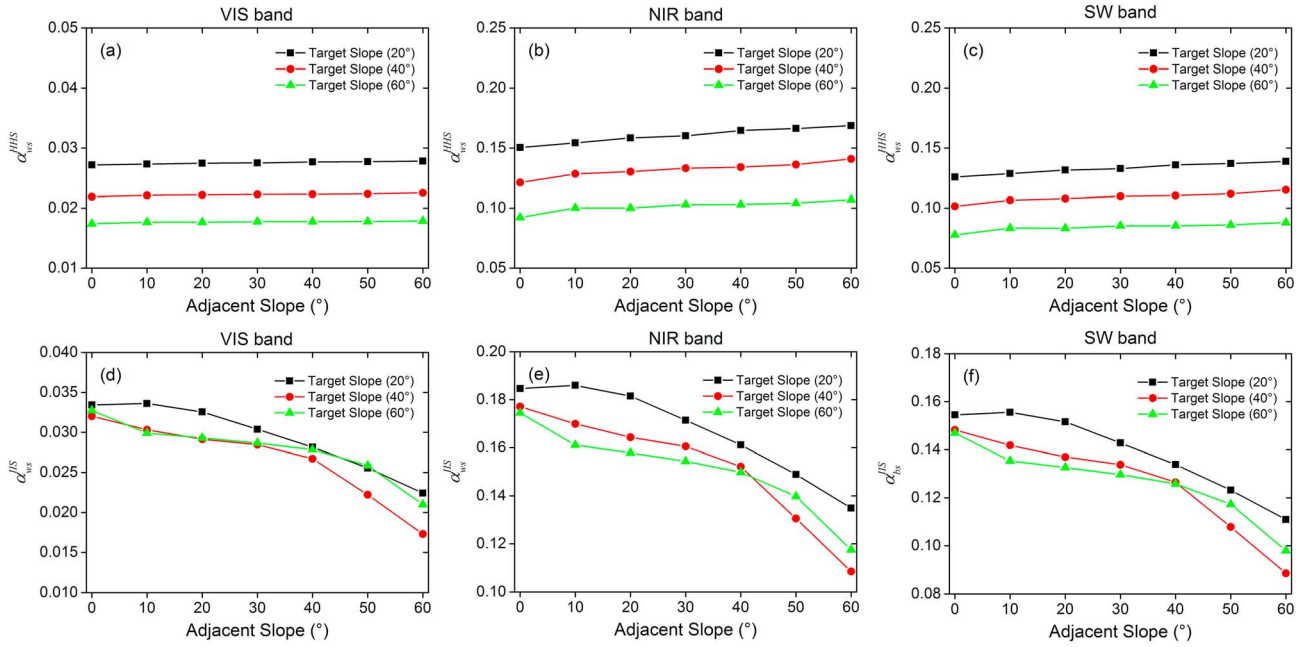

Figure 25. Effects of adjacent slope-reflected irradiance on α_{ws}^{HHS} and α_{ws}^{IIS}. VIS = visible; NIR = near infrared; SW = shortwave.

(38.4%), and 0.070 (38.7%) at the three broadbands. Nevertheless, adjacent slope-reflected irradiance should be considered in the albedo characterization for steep slopes, especially for snow-covered or ice-covered surfaces that have high reflectivity (Sirguey, 2009).

Compared with the previous studies, this paper thoroughly characterizes and quantifies three radiative flux components associated with their effective exposure to a radiometer in the albedo calculation. For example, previous studies usually neglect adjacent slope-reflected irradiance and imply that the effective exposure of a radiometer to the target surface in the reflected geometry is the same for both horizontal and slope-parallel radiometers (Weiser et al., 2016). These assumptions are not true since capturing effective exposure to a target surface is challenging in the course of a day, and it is therefore weighted by the radiometer with respect to the cosine law (Mannstein, 1985). On the other hand, this paper does not require the assumptions of isotropic surface reflection and isotropic illuminations, which are frequently used in current topographic corrections on albedo. Therefore, the surface anisotropic reflectance property and atmospheric radiative transfer model can be coupled in the albedo quantification by a surface BRDF model, such as the Li-Ross kernel-based model (Wanner et al., 1995) and vector linearized discrete ordinate RT atmospheric model (Huang et al., 2017).

Acknowledgments
We thank the relevant teams for providing the data sets used in this study. The in situ albedo data sets at ESM and ESR sites are provided by Roland Vogt from the University of Basel and available at http://www.map.meteoswiss.ch/. The in situ observations at CS-NF27 site are provided by Mathias W. Rotach from the University of Innsbruck and available at http://acinn.uibk.ac.at/research/atmospheric-dynamics/projects/i-box. We also thank the Editor and the anonymous reviewers for their beneficial comments and suggestions. This work was supported by the National Natural Science Foundation of China (41671363).

References

Anderson, R. G., Canadell, J. G., Randerson, J. T., Jackson, R. B., Hungate, B. A., Baldocchi, D. D., et al. (2011). Biophysical considerations in forestry for climate protection. *Frontiers in Ecology and the Environment*, *9*(3), 174–182. https://doi.org/10.1890/090179

Boussetta, S., Balsamo, G., Dutra, E., Beljaars, A., & Albergel, C. (2015). Assimilation of surface albedo and vegetation states from satellite observations and their impact on numerical weather prediction. *Remote Sensing of Environment*, *163*, 111–126. https://doi.org/10.1016/j.rse.2015.03.009

Chen, Y., Hall, A., & Liou, K. (2006). Application of three-dimensional solar radiative transfer to mountains. *Journal of Geophysical Research*, *111*, D21111. https://doi.org/10.1029/2006JD007163

Cherubini, F., Vezhapparambu, S., Bogren, W., Astrup, R., & Strømman, A. H. (2017). Spatial, seasonal, and topographical patterns of surface albedo in Norwegian forests and cropland. *International Journal of Remote Sensing*, *38*(16), 4565–4586. https://doi.org/10.1080/01431161.2017.1320442

Diner, D., Martonchik, J., Borel, C., Gerstl, S., Gordon, H., Knyazikhin, Y., et al. (1999). Level 2 surface retrieval algorithm theoretical basis. https://eospso.gsfc.nasa.gov/sites/default/files/atbd/ATB_L2Surface43.pdf

Diner, D. J., Martonchik, J. V., Kahn, R. A., Pinty, B., Gobron, N., Nelson, D. L., & Holben, B. N. (2005). Using angular and spectral shape similarity constraints to improve MISR aerosol and surface retrievals over land. *Remote Sensing of Environment*, *94*(2), 155–171. https://doi.org/10.1016/j.rse.2004.09.009

Dirmhirn, I., & Eaton, F. D. (1975). Some characteristics of the albedo of snow. *Journal of Applied Meteorology*, *14*(3), 375–379. https://doi.org/10.1175/1520-0450(1975)014<0375:SCOTAO>2.0.CO;2

Dozier, J., & Frew, J. (1990). Rapid calculation of terrain parameters for radiation modeling from digital elevation data. *IEEE Transactions on Geoscience and Remote Sensing*, *28*(5), 963–969. https://doi.org/10.1109/36.58986

Gastellu-Etchegorry, J.-P., Yin, T., Lauret, N., Cajgfinger, T., Gregoire, T., Grau, E., et al. (2015). Discrete Anisotropic Radiative Transfer (DART 5) for modeling airborne and satellite spectroradiometer and LIDAR acquisitions of natural and urban landscapes. *Remote Sensing*, *7*(2), 1667–1701. https://doi.org/10.3390/rs70201667

Georg, W., Albin, H., Georg, N., Katharina, S., Enrico, T., & Peng, Z. (2016). On the energy balance closure and net radiation in complex terrain. *Agricultural and Forest Meteorology*, *226*, 37–49. https://doi.org/10.1016/j.agrformet.2016.05.012

Georgescu, M., Lobell, D. B., & Field, C. B. (2011). Direct climate effects of perennial bioenergy crops in the United States. *Proceedings of the National Academy of Sciences*, *108*(11), 4307–4312. https://doi.org/10.1073/pnas.1008779108

Govaerts, Y., Lattanzio, A., Taberner, M., & Pinty, B. (2008). Generating global surface albedo products from multiple geostationary satellites. *Remote Sensing of Environment*, *112*(6), 2804–2816. https://doi.org/10.1016/j.rse.2008.01.012

Helbig, N., & Löwe, H. (2012). Shortwave radiation parameterization scheme for subgrid topography. *Journal of Geophysical Research*, *117*, D03112. https://doi.org/10.1029/2011JD016465

Hoch, S. W., & Whiteman, C. D. (2010). Topographic effects on the surface radiation balance in and around Arizona's Meteor Crater. *Journal of Applied Meteorology and Climatology*, *49*(6), 1114–1128. https://doi.org/10.1175/2010JAMC2353.1

Houspanossian, J., Giménez, R., Jobbágy, E., & Nosetto, M. (2017). Surface albedo raise in the South American Chaco: Combined effects of deforestation and agricultural changes. *Agricultural and Forest Meteorology*, *232*, 118–127. https://doi.org/10.1016/j.agrformet.2016.08.015

Huang, H., Qin, W., Spurr, R. J., & Liu, Q. (2017). Evaluation of atmospheric effects on land-surface directional reflectance with the coupled RAPID and VLIDORT models. *IEEE Geoscience and Remote Sensing Letters*, *14*(6), 916–920. https://doi.org/10.1109/LGRS.2017.2687702

Joerg, P. C., Weyermann, J., Morsdorf, F., Zemp, M., & Schaepman, M. E. (2015). Computation of a distributed glacier surface albedo proxy using airborne laser scanning intensity data and in-situ spectro-radiometric measurements. *Remote Sensing of Environment*, *160*, 31–42. https://doi.org/10.1016/j.rse.2014.12.017

Jonsell, U., Hock, R., & Holmgren, B. (2003). Spatial and temporal variations in albedo on Storglacia¨ ren, Sweden. *Journal of Glaciology*, *49*(164), 59–68. https://doi.org/10.3189/172756503781830980

Liang, S., Strahler, A. H., & Walthall, C. (1999). Retrieval of land surface albedo from satellite observations: A simulation study. *Journal of Applied Meteorology*, *38*(6), 712–725. https://doi.org/10.1175/1520-0450(1999)038<0712:ROLSAF>2.0.CO;2

Liang, S., Wang, K., Zhang, X., & Wild, M. (2010). Review on estimation of land surface radiation and energy budgets from ground measurement, remote sensing and model simulations. *IEEE Journal of Selected Topics in Applied Earth Observations and Remote Sensing*, *3*(3), 225–240. https://doi.org/10.1109/JSTARS.2010.2048556

Liu, J., Schaaf, C., Strahler, A., Jiao, Z., Shuai, Y., Zhang, Q., et al. (2009). Validation of Moderate Resolution Imaging Spectroradiometer (MODIS) albedo retrieval algorithm: Dependence of albedo on solar zenith angle. *Journal of Geophysical Research*, *114*, D01106. https://doi.org/10.1029/2008JD009969

Lucht, W., Schaaf, C. B., & Strahler, A. H. (2000). An algorithm for the retrieval of albedo from space using semiempirical BRDF models. *IEEE Transactions on Geoscience and Remote Sensing*, *38*(2), 977–998. https://doi.org/10.1109/36.841980

Mannstein, H. (1985). The interpretation of albedo measurements on a snow covered slope. *Meteorology and Atmospheric Physics*, *36*(1), 73–81. https://doi.org/10.1007/BF02269458

Mattar, C., Franch, B., Sobrino, J., Corbari, C., Jiménez-Muñoz, J., Olivera-Guerra, L., et al. (2014). Impacts of the broadband albedo on actual evapotranspiration estimated by S-SEBI model over an agricultural area. *Remote Sensing of Environment*, *147*, 23–42. https://doi.org/10.1016/j.rse.2014.02.011

Matzinger, N., Andretta, M., Gorsel, E. V., Vogt, R., Ohmura, A., & Rotach, M. (2003). Surface radiation budget in an Alpine valley. *Quarterly Journal of the Royal Meteorological Society*, *129*(588), 877–895. https://doi.org/10.1256/qj.02.44

Mayer, B., Hoch, S., & Whiteman, C. D. (2010). Validating the MYSTIC three-dimensional radiative transfer model with observations from the complex topography of Arizona's Meteor Crater. *Atmospheric Chemistry and Physics*, *10*(18), 8685–8696. https://doi.org/10.5194/acp-10-8685-2010

Milton, E. J., Schaepman, M. E., Anderson, K., Kneubühler, M., & Fox, N. (2009). Progress in field spectroscopy. *Remote Sensing of Environment*, *113*, S92–S109. https://doi.org/10.1016/j.rse.2007.08.001

Painter, T. H., Seidel, F. C., Bryant, A. C., McKenzie Skiles, S., & Rittger, K. (2013). Imaging spectroscopy of albedo and radiative forcing by light-absorbing impurities in mountain snow. *Journal of Geophysical Research: Atmospheres*, *118*, 9511–9523. https://doi.org/10.1002/jgrd.50520

Qu, Y., Liu, Q., Liang, S., Wang, L., Liu, N., & Liu, S. (2014). Direct-estimation algorithm for mapping daily land-surface broadband albedo from MODIS data. *IEEE Transactions on Geoscience and Remote Sensing*, *52*(2), 907–919. https://doi.org/10.1109/TGRS.2013.2245670

Román, M. O., Schaaf, C. B., Lewis, P., Gao, F., Anderson, G. P., Privette, J. L., et al. (2010). Assessing the coupling between surface albedo derived from MODIS and the fraction of diffuse skylight over spatially-characterized landscapes. *Remote Sensing of Environment*, *114*(4), 738–760. https://doi.org/10.1016/j.rse.2009.11.014

Rotach, M. W., Stiperski, I., Fuhrer, O., Goger, B., Gohm, A., Obleitner, F., et al. (2017). Investigating exchange processes over complex topography: The Innsbruck Box (I-Box). *Bulletin of the American Meteorological Society*, *98*(4), 787–805. https://doi.org/10.1016/j.rse.2009.11.014

Ryu, Y., Jiang, C., Kobayashi, H., & Detto, M. (2018). MODIS-derived global land products of shortwave radiation and diffuse and total photosynthetically active radiation at 5 km resolution from 2000. *Remote Sensing of Environment*, *204*, 812–825. https://doi.org/10.1016/j.rse.2014.12.017

Sailor, D. J., Resh, K., & Segura, D. (2006). Field measurement of albedo for limited extent test surfaces. *Solar Energy*, *80*(5), 589–599. https://doi.org/10.1016/j.solener.2005.03.012

Schaaf, C., Cihlar, J., Belward, A., Dutton, E., & Verstraete, M. (2009). *Albedo and reflectance anisotropy, ECV-T8: Assessment of the status of the development of standards for the terrestrial essential climate variables*. Rome, Italy: FAO.

Schaaf, C. B., Gao, F., Strahler, A. H., Lucht, W., Li, X., Tsang, T., et al. (2002). First operational BRDF, albedo nadir reflectance products from MODIS. *Remote Sensing of Environment*, *83*(1), 135–148. https://doi.org/10.1016/S0034-4257(02)00091-3

Schaaf, C. B., Li, X., & Strahler, A. H. (1994). Topographic effects on bidirectional and hemispherical reflectances calculated with a geometric-optical canopy model. *IEEE Transactions on Geoscience and Remote Sensing*, *32*(6), 1186–1193. https://doi.org/10.1109/36.338367

Schaepman-Strub, G., Schaepman, M., Painter, T., Dangel, S., & Martonchik, J. (2006). Reflectance quantities in optical remote sensing—Definitions and case studies. *Remote Sensing of Environment*, *103*(1), 27–42. https://doi.org/10.1016/j.rse.2006.03.002

Sellers, P., Meeson, B., Hall, F., Asrar, G., Murphy, R., Schiffer, R., et al. (1995). Remote sensing of the land surface for studies of global change: Models—algorithms—experiments. *Remote Sensing of Environment*, *51*(1), 3–26. https://doi.org/10.1016/0034-4257(94)00061-Q

Serrano-Ortiz, P., Sánchez-Cañete, E., Olmo, F., Metzger, S., Pérez-Priego, O., Carrara, A., et al. (2016). Surface-parallel sensor orientation for assessing energy balance components on mountain slopes. *Boundary-Layer Meteorology*, *158*(3), 489–499. https://doi.org/10.1007/s1054

Sicart, J. E., Ribstein, P., Wagnon, P., & Brunstein, D. (2001). Clear-sky albedo measurements on a sloped glacier surface: A case study in the Bolivian Andes. *Journal of Geophysical Research*, *106*(D23), 31,729–31,737. https://doi.org/10.1029/2000JD000153

Sirguey, P. (2009). Simple correction of multiple reflection effects in rugged terrain. *International Journal of Remote Sensing*, *30*(4), 1075–1081. https://doi.org/10.1080/01431160802348101

Stensrud, D. J. (2009). *Parameterization schemes: keys to understanding numerical weather prediction models*. Cambridge: Cambridge University Press.

Stiperski, I., & Rotach, M. W. (2016). On the measurement of turbulence over complex mountainous terrain. *Boundary-Layer Meteorology*, *159*(1), 97–121. https://doi.org/10.1007/s1054

Van Angelen, J., Lenaerts, J., Lhermitte, S., Fettweis, X., Munneke, P. K., Van den Broeke, M., et al. (2012). Sensitivity of Greenland ice sheet surface mass balance to surface albedo parameterization: A study with a regional climate model. *The Cryosphere*, *6*(5), 1175. https://doi.org/10.5194/tc-6-1175-2012

Wang, S., Trishchenko, A. P., & Sun, X. (2007). Simulation of canopy radiation transfer and surface albedo in the EALCO model. *Climate Dynamics*, *29*(6), 615–632. https://doi.org/10.1007/s00382-007-0252-y

Wang, Z., & Zeng, X. (2010). Evaluation of snow albedo in land models for weather and climate studies. *Journal of Applied Meteorology and Climatology*, *49*(3), 363–380. https://doi.org/10.1175/2009JAMC2134.1

Wanner, W., Li, X., & Strahler, A. (1995). On the derivation of kernels for kernel-driven models of bidirectional reflectance. *Journal of Geophysical Research*, *100*(D10), 21,077–21,089. https://doi.org/10.1029/95JD02371

Webster, C., Rutter, N., & Jonas, T. (2017). Improving representation of canopy temperatures for modeling subcanopy incoming longwave radiation to the snow surface. *Journal of Geophysical Research: Atmospheres*, *122*, 9154–9172. https://doi.org/10.1002/2017JD026581

Weiser, U., Olefs, M., Schöner, W., Weyss, G., & Hynek, B. (2016). Correction of broadband snow albedo measurements affected by unknown slope and sensor tilts. *The Cryosphere*, *10*(2), 775–790. https://doi.org/10.1175/2009JAMC2134.1

Wen, J., Liu, Q., Liu, Q., Xiao, Q., & Li, X. (2009). Parametrized BRDF for atmospheric and topographic correction and albedo estimation in Jiangxi rugged terrain, China. *International Journal of Remote Sensing*, *30*(11), 2875–2896. https://doi.org/10.1080/01431160802558618

Wen, J., Zhao, X., Liu, Q., Tang, Y., & Dou, B. (2014). An improved land-surface albedo algorithm with DEM in rugged terrain. *IEEE Geoscience and Remote Sensing Letters*, *11*(4), 883–887. https://doi.org/10.1109/LGRS.2013.2280696

Widlowski, J. L., Taberner, M., Pinty, B., Bruniquel-Pinel, V., Disney, M., Fernandes, R., et al. (2007). Third radiation transfer model Intercomparison (RAMI) exercise: Documenting progress in canopy reflectance models. *Journal of Geophysical Research*, *112*, D09111. https://doi.org/10.1029/2006JD007821

Wu, X., Wen, J., Xiao, Q., Yu, Y., You, D., & Hueni, A. (2017). Assessment of NPP VIIRS albedo over heterogeneous crop land in Northern China. *Journal of Geophysical Research: Atmospheres*, *122*, 13,138–13,154. https://doi.org/10.1002/2017JD027262

Zhang, Y., Xiao, Q., Wen, J., You, D., Dou, B., & Tang, Y. (2017). Review on spectral libraries: Progress and application. *Journal of Remote Sensing*, *21*, 12–26. https://doi.org/10.11834/jrs.20175324

Erratum

The second institutional affiliation has been corrected to "College of Resources and Environment, University of Chinese Academy of Sciences, Beijing, China" since the paper was originally published. This updated version may be considered the authoritative version of record.